Masters Thesis

Bistatic SAR data acquisition and processing using SABRINA-X, with TerraSAR-X as the opportunity transmitter

Author: Muhammad Adnan Siddique
Director: Prof. Dr. Antoni Broquetas

July, 2010

Universitat Politènica de Catalunya (UPC)
Department of Signal Theory and Communications (TSC)
Barcelona

Contents

Abstract

This thesis investigates the acquisition and processing of Bistatic SAR data using SABRINA-X, and with TerraSAR-X as the transmitter of opportunity. SABRINA-X is an X-band receiver system that has been recently designed at the UPC Remote-Sensing Laboratory, while TerraSAR-X is a German satellite for SAR-based active remote-sensing.

Prior to the particular case of acquiring TerraSAR-X signals, the hardware aspects of SABRINA-X have been investigated further, and improved as necessary (or suggested for up-gradation in future). Two successful data acquisitions have been carried out, to obtain bistatic SAR images of the Barcelona harbor, with the receiver set-up at the close-by Montjuïc hill. Each acquisition campaign necessitated an accurate prediction of the satellite overpass time and precise orientation of the antennas to acquire the direct signal from the satellite and the backscattered signals off the viewed terrain.

The thesis also investigates the characteristics of the acquired signals, which is critical as regards the subsequent processing for imaging and interferometric applications. The hardware limitations, combined with ‘off-nominal’ transmissions of the satellite, necessitate improved range processing of the acquired signals. The thesis expounds the possible range compression techniques, and suggests ways for improved compression, thereby improving the quality of the subsequently processed images. [1]

[1] The results obtained under this thesis work have been presented at the European SAR conference (EUSAR) 2010, Aachen, Germany, and accepted for publication at the IEEE Geoscience and Remote Sensing Symposium (IGARSS) July 2010.

Introduction

'Sensing' is a human instinct: we need to explore our surroundings, and apprise ourselves of the hidden entities around us. Equipped with the basic senses of sight, hearing, smell and touch, the aboriginal man groped in the wilderness, perceptive of the sounds of a hunt for food or those of a fearful beast that may endanger his life. The nomadic night watchman kept a look-around for a possible enemy attack, and the early pharmacist acutely smelt his potions to make the right medicine. Times have changed enormously, evolving from the prehistoric days of cave-life to the modern age when humans are launching sensors in space to search for life elsewhere in the universe. Apart from the remarkable growth of the sensing techniques, the very 'need' of sensing has grown enormously too; especially over the last century, as we realize it's implications in almost all walks of life, be it navigation, meteorology, oceanography, forestry, hydrology, agriculture or military reconnaissance.

Keeping in view the enormity of the universe we live in, sensing with contact or with close proximity is usually not feasible. It leads us to the idea of 'remote-sensing'; which in a scientific context, refers to the set of techniques employed to gather data and information about the characteristics of an object, without physical contact or close proximity, rather by collecting the Electromagnetic (EM) radiation associated to the object. The radiation may be radio, microwave, infra-red, visible, ultra-violet, X-ray etc. It may be a self-emission from the object or a scattered return of the incident radiation.

Remote-sensing systems are space-borne, air-borne as well as ground-based. Space-borne systems are more important in the context of global sensing, e.g. monitoring global climate variations or oceanography. Sensors in space cover much larger territories compared to the ground-based or air-borne. Remote-sensing techniques can be broadly classified as active or passive. Active remote sensing involves the transmission of EM radiation towards the target; the backscattered signals are received and processed to infer the physical characteristics of the target. Such active remote sensing instruments include Side-looking air-borne radar (SLAR), Synthetic Aperture Radars (SAR), Scatterometers, Altimeters etc. Contrarily, passive systems do not involve a transmitter of EM radiation. Instead a receiver collects the inherent radiation emission from the object owing to the physical temperature of the object. Radiometers refer to such passive receivers.

SAR-based space-borne sensing has emerged as a very useful technique for Earth observation over the last few decades, primarily due to the fact that they provide high resolution terrain images of large territories independently of weather conditions. SEASAT was the first space-borne SAR mission, launched in 1978 [1]. Since then, a number of SAR missions have been launched over time, by different space agencies across the globe, e.g. ENVISAT and ERS-1/2 (launched by the European Space Agency (ESA). TerraSAR-X was launched in 2007 by the German Aerospace Center. These missions have made available a good supply of SAR data, which has subsequently helped in grooming a number of SAR-derived techniques for improved inferences extending to wider applications. These techniques include SAR interferometry (InSAR), differential InSAR (DInSAR), polarimetric SAR (pol-SAR), and polarimetric InSAR. With intensive research, most of these techniques have reached maturity in the monostatic case (where both the transmitter and receiver are borne on the same platform), however, the bistatic and multistatic variants (where the transmitter and the receiver are not borne on the same platform, and there may be more than one receiver) of these techniques have opened new lines of research [2].

The Remote Sensing Laboratory (RSLab) at Universitat Politènica de Catalunya (UPC) is rendering intensive research efforts along these lines. A C-Band receiver has been developed to investigate bistatic configurations with fixed ground-based receivers and orbitals sensors (such as ENVISAT and ERS-1/2) as transmitters of opportunity. A number of successful data acquisition campaigns have already been conducted. It has been named SABRINA (**SA**R **B**istatic **R**eceiver for **Interferometric A**pplications). The X-band version of this system has recently been designed at the lab [3], and is undergoing improvements. It is referred to as SABRINA-X.

This thesis, conducted at the RSLab, investigates the acquisition and processing of Bistatic SAR data, using SABRINA-X and with TerraSAR-X as the transmitter of opportunity. This report presents the work done as part of the thesis. It opens with an introduction to the fundamentals of synthetic aperture radar. The geometry of bistatic Synthetic Aperture Radar (SAR) is discussed in comparison to the mono-static case, highlighting the subsequent processing concerns in general. The following chapter presents the hardware features of SABRINA-X, especially those in direct relation to the acquisition and the processing of data, e.g. the IF/IQ acquisition modes, the limitations of digitizer memory, channel gains, etc. An overview of TerraSAR-X is also provided. The next chapter discusses the campaigns for the acquisition, focusing on the experimental set-up for a successful acquisition. The subsequent chapters focus on the range processing concerns: the acquired range chirp signals are analyzed and their characteristics such as the chirp rate and pulse length are precisely estimated. The chapter on range processing discusses the issues associated with range compression of the acquired signals, and suggests ways for improvement. The final chapter presents the results, highlighting the improvements realized.

1. SAR Fundamentals

The invention of radar owes to several contributors over time; however, the earliest conception of the idea to detect the presence of a remote object with the help of radio waves is patented to the German engineer, Christian Hülsmeyer (1881—1957) [4]. The process of detection relied on the principle of radio wave reflection from metal and dielectric objects. It was an easy realization that this method can also be used to find the distance of the remote object from the transmit station, by measuring the elapsed time between the transmitted radio signal and the corresponding echo received after the reflection of the signal from the object. The word RADAR is, therefore, an acronym of the phrase '**Ra**dio **D**etection **A**nd **R**anging'.

Radar systems experienced tremendous development independently in different countries across the globe prior to the Second World War [5]. They were used as a tool to detect and track targets such as aircraft and ships. Some radars were used for military reconnaissance as well. The use of radio waves for detection allowed military operations even at night times. As the use of radar was primarily military during this time, the focus of system design remained to be the enhancement of accuracy/reliability of detection and tracking. It was, however, quite late even after the end of the war that radars began to be used for non-military/part non-military purposes as well, such as remote sensing.

Remote-sensing refers to the measurement of an object's characteristics without any physical contact or close proximity. It is exemplified by terrain-mapping, which originally began with aerial photographic techniques; however, these techniques were marred by natural limitations such as occlusion due to cloud cover, absence of sunlight at night time or an unfavorable solar illumination. Remote-sensing with the help of electromagnetic waves (radio or microwaves) could surely circumvent such limitations of environment. Radars were hence-forth employed for this purpose. Side-looking Air-borne Radars (SLAR) were developed for terrain mapping, and they proved useful in mapping areas that were perpetually cloud-covered. The radar, being air-borne, flies over the territory to be mapped, illuminating it with EM waves, and collecting the return signals which are afterward processed to generate the terrain (reflectivity) image. SLARs have, however, suffered from inadequate azimuth (along the flight track) resolution. Increasing the resolution necessitates use of very large antennas which are impractical. Moreover, the resolution decreases as the height of the radar (the range) above the terrain increases. These factors led the researchers to invent a new technology, later referred as '**S**ynthetic **A**perture **R**adar (**SAR**)'.

1.1. Synthetic Aperture Radar (SAR)

It was practically demonstrated for the first time in 1953 that high azimuth resolution can be achieved without the need of impracticably large antenna and over-riding the limitation of resolution dependence on range [6]. This system is the SAR, which 'synthetically' generates a large antenna aperture that serves to significantly improve the azimuth resolution. SAR is also a side-looking system like the SLAR; it, however, relies on more sophisticated data processing.

Considering a SLAR system, the azimuth resolution δ_{az} depends on the 3 dB beam-width (along the azimuth direction) of the antenna θ_{3dB} , and the distance (i.e. slant range) R_s between the ground target and the radar sensor. It is given by:

$$\delta_{az} = \theta_{3dB} \cdot R_s$$

With 3 cm wavelength, and an antenna size of 5 m, the azimuth resolution is around 30 m for a range of 3 km. If, however, the range increases to 10 km, the resolution decreases to 100 m. This phenomenon owes to the fact that as the range increases, the EM waves spread over a wider geometric expanse, thereby reducing azimuth resolution. A SAR system, however, does an end run around this fundamental limitation. A SAR system, while it flies over an object, illuminates it with radiation and continues to collect the backscattered radiation for as long as the object remains within the radar antenna's main beam. The received echoes are coherently integrated to generate a 'synthetic' aperture L_{sa} , which is significantly large compared to the real antenna aperture, and hence a large azimuth resolution is realized. Moreover, as the range increases, the ground object experiences a larger illumination time due to wider geometric spreading of antenna's main beam. Although it is expected that as with SLAR, wider geometric spreading of the main beam would cause loss of resolution; however, this factor is countered by the fact that now the illumination time has also increased and therefore, the synthetic aperture has further increased. This leads us to the fact that SAR systems can obtain azimuth resolutions that are independent of the distance to the target. In fact, the theoretical azimuth resolution of SAR, $\delta_{az,SAR}$ is one half of the real antenna aperture along the azimuth direction.

The significantly better resolution combined with independence from range are the features that augment the ability of SAR to perform high resolution remote-sensing as opposed to SLAR.

1.1.1. SAR Geometry

Figure (1.1.1) shows the side-looking geometry of a (monostatic) SAR. The SAR sensor borne on a satellite platform files over the territory to be 'sensed', illuminating the terrain underneath. The direction of flight is referred to as the '*azimuth*' or '*along-track*' direction. The distance from the sensor to the ground is target terrain is the 'slant range, R', and it's on ground projection is the 'range'. The sensor collects the return signals, and upon coherent processing, a synthetic aperture L_{sa}. The angle of incidence of the illumination from the satellite is θ_{inc} , while θ_{3dB} is the along-track transmit antenna beamwidth.

1.1.2. Signals in range and azimuth

A SAR system, analogous to a conventional pulsed radar system, evaluates the range by finding the time delay between the transmission of the pulse and the reception of the corresponding

Figure 1.1.1.: Sidelooking Geometry of a monostatic SAR

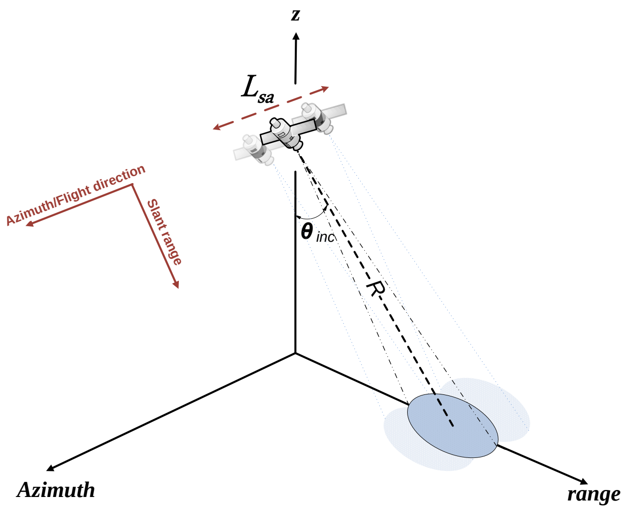

echo. Considering the time delay is T_{delay} , we get

$$r_s = \frac{c \cdot T_{delay}}{2} \tag{1.1.1}$$

where c is the speed of light. In order to detect two closely spaced objects as two separate entities, i.e. as 'resolved' in distance, the echos received for each must not overlap. Therefore, the echo pulses from each target must be separated in time from one another by at least the duration of the pulse. Hence the range resolution in slant range is given by

$$\delta_{sr} = \frac{c \cdot T_{pulse}}{2} \backsimeq \frac{c}{2 \cdot B_{pulse}} \tag{1.1.2}$$

where T_{pulse} is the duration of the pulse, and $B_{pulse}$is the corresponding bandwidth. An increase in range resolution necessitates an increase in bandwidth of the pulse, which can be achieved by reducing the pulse duration; however, a decrease in pulse duration leads to a corresponding decrease in the radiated energy which in turn deteriorates the probability of detection. The alternative approach is to use pulse compression. Instead of reducing the pulse duration, the pulse is linearly frequency modulated to yield a 'chirp' signal which has a higher bandwidth. The instantaneous phase of the signal is given by

$$\phi_r(t) = \pi \cdot k_r \cdot t^2 \tag{1.1.3}$$

while the instantaneous frequency is

$$f_r(t) = k_r \cdot t \tag{1.1.4}$$

with $-\frac{T_{pulse}}{2} \leq t \leq \frac{T_{pulse}}{2}$. The range signal is, therefore, a linearly frequency modulated 'Chirp' signal, which is transmitted in pulses at a regular frequency, known as the pulse-repetition-

Figure 1.1.2.: Chirp signal in Range

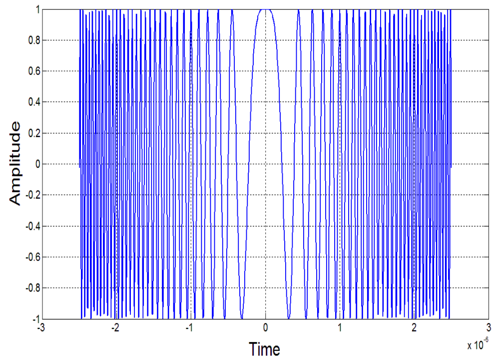

Figure 1.1.3.: Geometry depicting the time-variation of distance leading to phase change, and hence frequency modulating the signal in azimuth: Doppler Effect

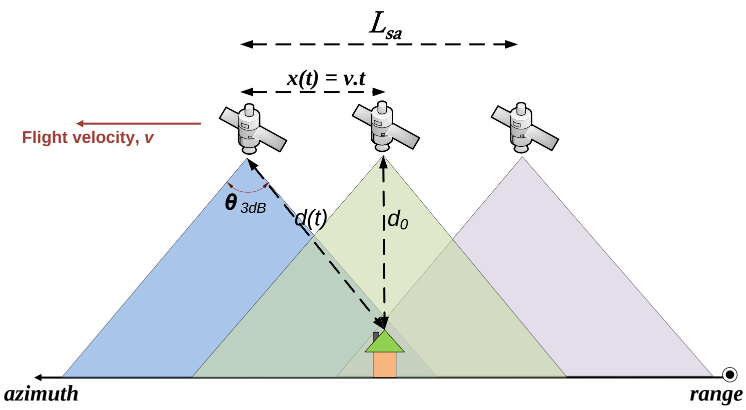

frequency(PRF). The bandwidth of this chirp is given by

$$B_r = \mid k_r \mid \cdot T_{pulse} \tag{1.1.5}$$

A negative value of k_r implies a down chirp, and vice-versa. An example down chirp signal is shown in Figure (1.1.2).

The radar's flight over the terrain to be mapped in fact induces a relative velocity between the radar and the target object. The component of this relative velocity is non-zero in the azimuth direction. Doppler effect is the natural outcome. SAR signal in azimuth are hence frequency modulated owing to the Doppler phenomenon.

While the radar is flying above and the target is being illuminated, there is a continuous variation in the distance to the target. Figure (1.1.3) depicts the geometry with three time instants of a space-borne SAR flying along the azimuth, illuminating a target underneath. The phase of the

Figure 1.1.4.: Squinted antenna beam, leading to Doppler centroid

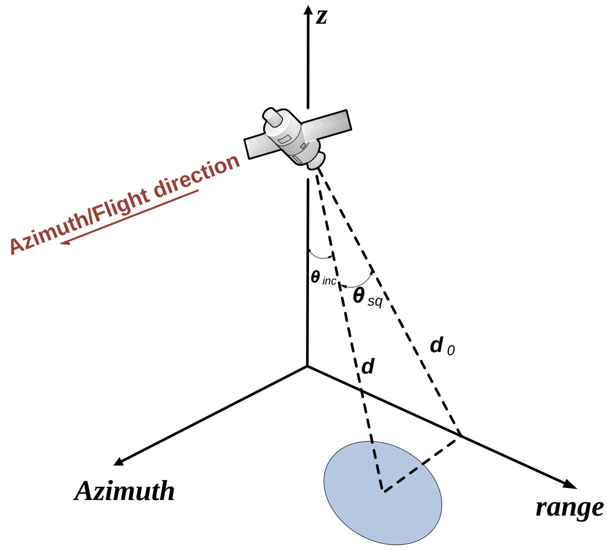

signal is changing as a consequence of time-variation of distance $d(t)$ between the radar and the target. The instantaneous value of the phase is given by

$$\phi_{az}(t) = -\frac{4\pi}{\lambda} \cdot d(t) \tag{1.1.6}$$

and the distance is

$$d(t) = \sqrt{d_0^2 + v^2 \cdot t^2} \tag{1.1.7}$$

A Taylor approximation, and subsequent derivation, referred to [7], yields the following instantaneous value of frequency

$$f_{az}(t) = -\frac{2 \cdot v^2}{\lambda \cdot d_0} \cdot t = k_{az} \cdot t \tag{1.1.8}$$

where $k_{az}$is the Doppler rate.

The frequency is a linear function of time, which is analogous to the case of SAR signal in range. The azimuth signal is, therefore, also a 'chirp'; however, this chirp is naturally induced contrary to the scenario of range signal where the signal is purposefully modulated as a chirp to increase its bandwidth. The chirp signals in range and azimuth together yield a 2-Dimensional chirp signal.

The relation (1.1.8) is slightly modified in case the transmit antenna beamwidth is *'squinted*', as shown in the figure 1.1.4, and the instantaneous azimuth frequency is

$$f_{az}(t) = f_{dc} + k_{az} \cdot t \tag{1.1.9}$$

where

$$f_{dc} = \frac{2 \cdot v \cdot \sin(\theta_{sq})}{\lambda} \tag{1.1.10}$$

Figure 1.1.5.: Range resolution

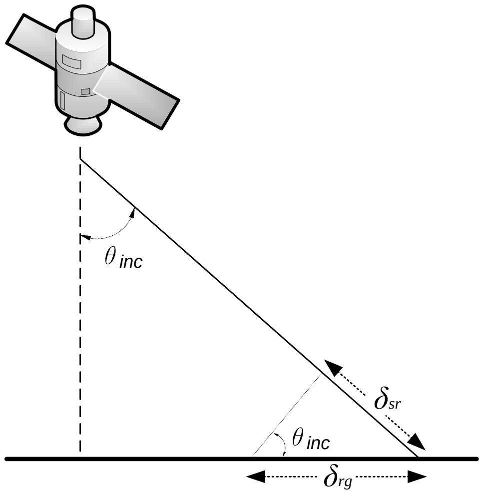

The Doppler bandwidth is

$$B_{doppler} = f_{az,max} - f_{az,min} \tag{1.1.11}$$

where $f_{az,max}$ and $f_{az,min}$ are the maximum and the minimum values of the azimuth frequency.

1.1.2.1. Range resolution

The resolution in slant range is referred to the equation (1.1.2). However, the on-ground range resolution δ_{rg} is a projection of the slant range resolution, as shown in the figure (1.1.5).

$$\delta_{rg} = \frac{\delta_{sr}}{\sin(\theta_{inc})} = \frac{c}{2 \cdot B_{pulse} \cdot \sin(\theta_{inc})} \tag{1.1.12}$$

1.1.2.2. Azimuth resolution

Referring to figure (1.1.3), a synthetic aperture L_{sa} is synthesized corresponding to the length of time the target remains illuminated while the sensor flies overhead. This time is called the 'illumination time'. In a theoretical sense, the synthetic aperture is equal to the along-track distance traversed by the sensor during the illumination time, which corresponds to the length of the along-track footprint. We get

$$L_{sa} = \theta_{3dB} \cdot d_0 = \frac{\lambda}{l_{az}} \cdot d_0 \tag{1.1.13}$$

where $l_{az}$is the real antenna aperture of the transmit antenna, along the azimuth direction. The 'synthetic beamwidth' is then

$$\theta_{sy} = \frac{l_{az}}{2 \cdot d_0} \tag{1.1.14}$$

and therefore the corresponding azimuth resolution is

$$\delta_{az} = \theta_{sy} \cdot d_0 = \frac{l_{az}}{2} \tag{1.1.15}$$

which is independent of the range.

1.2. Bistatic Synthetic Aperture Radar

Multistatic and Bistatic SAR systems are an emerging research field. In a bistatic SAR system, contrary to the monostatic case, the transmitter and the receiver are borne on different platforms, and they follow different trajectories, which may be completely independent from each other. In some cases, using a bistatic configuration is more beneficial than the monostatic, e.g with a bistatic system, it may be possible to generate good quality data where the performance of a typical orbital monostatic geometry is severely worsened by foreshortening, which degrades the ground-range resolution, or by layover effects. In multistatic systems, the use of multiple receivers placed at different locations allows observing the scene from different points of view. Such a configuration makes possible the extraction of 3D vector of movement [2]. It has to appreciated that the cost of deploying a monostatic system with similar capabilities would be far higher.

The following subsections consider the particular case of bistatic SAR system with a fixed-receiver, and a space-borne transmitter which synthesizes the synthetic aperture along it's orbital track.

1.2.1. Bistatic SAR Geometry

There are two typical geometries: *forward scattering* and *backscattering*. In a backscattering case, both the transmitter and the receiver are on the same side of the viewed scene; however, for the forward scattering case, the viewed scene is in between the transmitter and the receiver, such that the signals collected by the receiver are those which have been scattered away from the incidence side of the scene.

Figure 1.2.1 shows the two scenarios. The angles $\theta_{inc}$and θ_r are the incidence angles of the transmitter and the receiver respectively. The angle α is the slope of the local terrain; R_t is the distance of the transmitter to the target, and R_r is the distance of the receiver from the target.

1.2.2. Bistatic SAR signals in range and azimuth

As for the monostatic case, the signal in range is a linear FM 'chirp' signal, which allows achieving a higher pulse bandwidth compared to an un-modulated pulse signal. The formulation of the range resolution is, however, not the same as it is affected by the geometry, as expressed

Figure 1.2.1.: Backscattering (blue) and forward scattering (red) bistatic SAR geometries

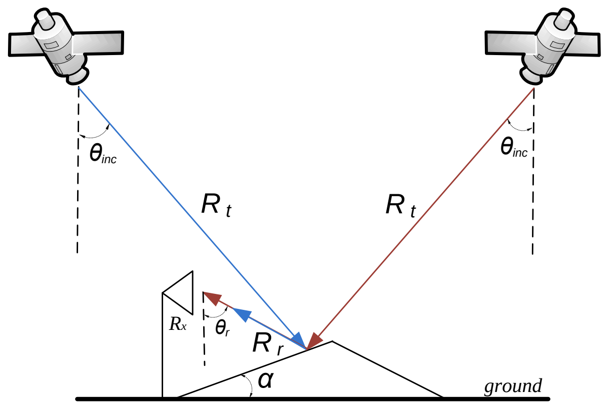

in section 1.2.2.1. The variation of the distance between the receiver and the transmitter is also different, as highlighted in the figure 1.2.2 . The equation 1.1.7 is changed to

$$d(t) = \sqrt{d_1^2 + v^2 \cdot t^2} + d_2 \tag{1.2.1}$$

1.2.2.1. Range resolution

For a monostatic configuration, the points that belong to the same range form isorange spheres centered at the position of the transmitter (which is also the position of the receiver). However, in a bistatic geometry, the isorange surfaces are the loci of points where the sum of the distances to transmitter and the receiver is a constant; this implies that the isorange surfaces are ellipsoids with the transmitter and the receiver as the foci [2]. Considering that the local terrain has slope α_t with respect to the transmitter and α_t with respect to the receiver, the ground-range resolution is

$$\delta_{rg,bistatic} = \frac{c}{B_{pulse} \cdot (\sin(\theta_t - \alpha_t) + \sin(\theta_r - \alpha_r))} \tag{1.2.2}$$

In a forward scattering scenario, the angles θ_t and θ_r have opposite signs. For the case when the transmitter is space-borne, and the receiver is fixed on ground, the local slopes α_t and α_t are very similar, i.e. $\alpha_t \approx \alpha_r = \alpha$. Moreover, referring to figure 1.2.1 for the back-scattering case, if the angles θ_{inc} and θ_r become the same, the bistatic ground-range resolution becomes the same as the monostatic as in equation 1.2.2.1

1.2.2.2. Azimuth resolution

The azimuth resolution of a SAR system can also be related to the Doppler bandwidth and the velocity of the moving platform. Keeping in view the frequency-time duality, a Doppler

Figure 1.2.2.: Bistatic SAR range variation with time

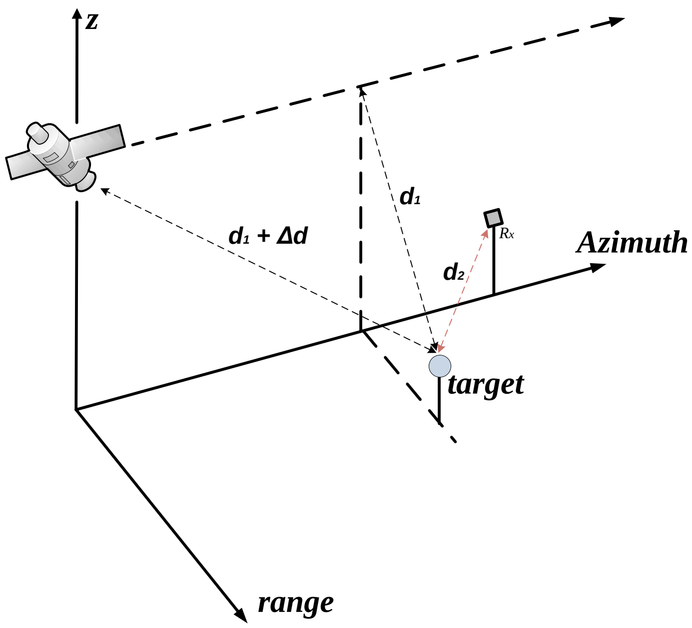

bandwidth of $B_{doppler}$ can be inverted to obtain a temporal resolution, and when yields the azimuth resolution when multiplied by the platform velocity [8], i.e.

$$\delta_{az,bistatic} = \frac{v}{B_{doppler,bistatic}} \tag{1.2.3}$$

For the monostatic case, the Doppler bandwidth is related to the two-way antenna azimuthal beamwidth of the transmit-receiver antenna $\theta_{3dB,2way}$. In a bistatic scenario, since the receive antenna is not borne on the same platform as the transmitter, we are concerned a one-way transmit antenna beamwidth, $\theta_{3dB,1way}$. Approximating the beam pattern with a Gaussian function [8], the ratio between the one-way and the two-way beam patterns is $\sqrt{2}$. This implies that in a bistatic scenario, there is loss of resolution by a factor of two due to one-way beam pattern instead of two-way beam patter as for the monostatic, but since the one-way beam pattern is wider and therefore, the illumination time is more, compensating the loss to some extent. We get,

$$\delta_{az,bistatic} = \sqrt{2} \cdot \delta_{az,monostatic} \tag{1.2.4}$$

1.3. SAR processing

This section briefly highlights the basic processing steps for a SAR system in general. A SAR system collects an enormous amount of data during its flight mission. The data is mostly processed offline. There are different algorithm varying in complexity and efficiency to process the data and generate accurate and reliable images of the mapped terrain; each algorithm, however, incorporates some ways to undertake the following procedures which are fundamental to SAR data processing.

1.3.1. Range compression

SAR transmits linear FM modulated pulse signal, i.e. the chirp. When this pulse is filtered with a 'matched filter', the result is a narrow pulse in which all the pulse energy is concentrated. Therefore, when a matched filter is applied to the received echo, a narrow pulse is realized allowing better range resolution while at the same time offering the best possible signal-to-noise ratio. This matched filtering is called range compression . Matched filter can be generated with the replica of the transmitted signal, and it may be referred as the range reference function. The matched filtering of the received echo is achieved by convolving it with range reference function. Range compression can be done efficiently in frequency domain (as opposed to time domain which takes a significantly longer time) using fast Fourier transform techniques.

1.3.2. Range cell migration (RCM)

An accurate inference of the target position in the range direction is hampered by the fact that as the radar flies above, the echos from the target are received with a varying time delay due to time-variation in the distance from the target to the radar (as mentioned in the last section). The system infers a changing range, although the target is fixed in the range direction. This problem is referred as range cell migration. It must be corrected by the SAR data processor. After range compression, the signal energy from a point target follows a trajectory in the two-dimensional SAR data (in range and azimuth). Instead of a trajectory, the point target must have a constant position in range. Range cell migration correction (RCMC) is the procedure to correct the changing range delay to the point target such that the target appears at constant range instead of following a trajectory in range-azimuth plane. Different algorithms have been formulated to correct range cell migration, such as the *Range-Doppler Algorithm* and the *Chirp-Scaling Algorithm.*

1.3.3. Azimuth compression

Azimuth compression refers to matched filtering of the azimuth signal. An azimuth reference function is generated which is then convolved with the received signal to generate the image data. This convolution in time-domain is generally carried (as multiplication) in frequency domain. The azimuth signal is a chirp, and therefore when matched filter, it yields a narrow pulse analogous to range compression. Azimuth and range compression together lead to a narrow 2-Dimensional pulse as the impulse response of the SAR processor.

1.4. Application of SAR systems

SAR has indeed emerged as a standard tool for Earth observation. Many SAR missions have been launched over the last few decades. The application areas of these missions can be briefly stated as:

- Topography: providing terrain maps, Digital Elevation Models (DEMs) of the Earth‘s surface
- Oceanography: measuring wind speeds, ocean currents
- Glaciology: measuring the slight movements of glaciers, snow wetness
- Agriculture: classifying crops, soil moisture
- Geology: discriminating terrain types, relief features deformation due to natural disasters (floods, earthquake, and volcanic eruption)
- Forestry: estimating biomass and forest height, monitoring deforestation
- Environment monitoring: monitoring oil spills, urban growth
- Military: aiding in military strategies, reconnaissance, surveillance

2. Acquisition System

This chapter presents a discussion of the acquisition system, comprising of TerraSAR-X as the transmitter of opportunity and SABRINA-X as the fixed ground-based X-band SAR receiver.

2.1. Transmitter of Opportunity: TerraSAR-X

TerraSAR-X is proudly called the ‘German Eye in the Space’ [9]. It is an Earth observation satellite launched on June 15, 2007 from the ‘Russian Baikonur Cosmodrome’ (in Kazakhstan). The German Aerospace Center (DLR), the German Federal Ministry of Education and Research and Astrium GmbH are partners in carrying out this mission. The mission became fully operational since January 7, 2008. It is offering remote-sensing capabilities that were previously unavailable. It has been a big success story thus far, bringing Germany at a leading position among the countries pursuing space technology; or in the words of DLR, ‘the world leader in Earth Observation’ [9].

The objective of the TerraSAR-X mission is to provide value-added SAR data for scientific, commercial and research-and-development purposes. It aims to provide very high quality images of the Earth‘s surface, combined with very high accuracy, independently of the weather conditions and presence/absence of sunlight. It offers very high ground resolution (significantly more than the earlier SAR missions), and a possibility of observation over longer time spans; it is capable of providing detailed ground features, serving application needs such as more detailed DEMs, more information regarding forestry, relief features’ deformation due to earthquakes or floods, etc.

2.1.1. Satellite orbit

TerraSAR-X satellite orbits around the Earth in a sun-synchronous, dusk-dawn, low-earth orbit (LEO), with zero eccentricity and an inclination angle of 97.44 degrees (which implies a nearly polar orbit). The altitude is 514 km [10]. It has an 11 days repeat period. Due to swath overlay, a revisit time of 2.5 days can be achieved [10].

2.1.2. Modes of operation

The primary payload of TerraSAR-X is the X-Band SAR sensor. The center frequency is 9.65 GHz. It is capable of operating in different modes (spotlight, scanning, stripmap) each having

Figure 2.1.1.: TerraSAR-X in space (courtesy DLR)

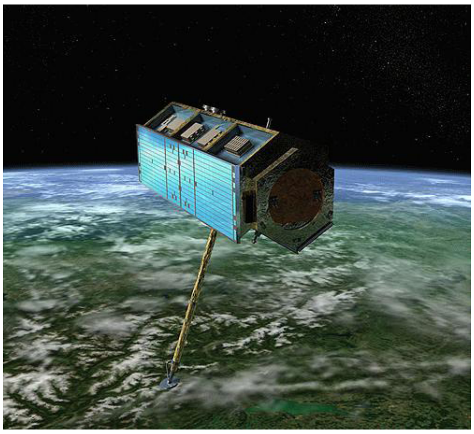

different swath width and resolution. Hence, the use of the sensor can be tailored to the need of the application. Moreover, the sensor is full-polarimetric (operates with quad polarizations) and is capable of interferometry as well. The different modes of operation are highlighted below:

- Stripmap: The sensor continuously illuminates the swath, without interruptions, while it is flying. The antenna beams sweeps along the sensor. The illuminated area on ground is 30 km wide and 50 km long, with a resolution of 3m [10].
- Spotlight: The ground illumination is not continuous; instead it is focused on a target area and the antenna beam does not sweep along the sensor as it flies. The antenna beam illuminates a fixed area 10 km wide and 5 km long. The illumination time is longer compared to the stripmap mode, and hence a higher resolution of 1 m is achieved [10]. However, since the sensor has flown past while the antenna is still fixed to the same target area, the coverage is not continuous. The next patch of illuminated area is not adjacent to the first. Spotlight mode turn has two variants with different values of azimuth resolution, called *Spotlight mode* (SL) and *High Resolution Spotlight* (HS).
- ScanSAR: In this mode, a very wide swath is illuminated, but correspondingly a reduced illumination time is served. The swath is split into sub-swaths and the beam switches from one to the next in quick succession. The resolution obtained, with illuminating a ground area 100 km wide and 150 km long, is 18 m [10].

2.1.3. System specifications

The general system specifications (referred to [11]) of TerraSAR-X are briefly stated in the table 2.1.1, for a quick reference.

Table 2.1.1.: TerraSAR-X: System specifications (quick reference)

Parameter	*Value*
Center frequency	9.65 GHz
Operational bandwidth	typically 150 MHz (or experimentally 300 MHz)
Peak radiated power	2260 W
Polarizations	HH, VH, HV, VV
Antenna type	X-band phased array with beam-steering
Nominal antenna look direction	right
Pulse repetition frequency (PRF)	2.2 KHz - 6.5 KHz

(a) X-Band sensor specifications

Parameter	*Value*
Inclination	97.44°
Nominal orbit height at the equator	approx 514 km
Orbits per day	15 $2/11$
Revisit time (orbit repeat cycle)	11 days

(b) Orbit characteristics

Parameter	*Value*
Swath width (ground range)	approx 30 km
Acquisition length	max 1650 km
Incidence angle (full performance)	20°- 45°
Azimuth resolution	3 m (single polarization) 6 m (dual polarization)
Ground range resolution	1.7 m @ 45° incidence angle 3.5 m @ 20° incidence angle
Polarization	HH or VV (single) HH/VV, HH/HV, VV/HV (dual)

(c) Stripmap mode characteristics

Parameter	*Value*
Scene extension	10 km (azimuth) $\times$ 10 km (range)
Incidence angle (full performance)	20°- 55°
Azimuth resolution	2 m (single polarization) 4 m (dual polarization)
Ground range resolution	1.5 m @ 55° incidence angle 3.5 m @ 20° incidence angle
Polarization	HH or VV (single) HH/VV (dual)

(d) Spotlight mode characteristics

2.2. Receiver System: SABRINA-X

The eagerness to pursue research in bistatic SAR applications gave birth to the idea of developing a fixed ground-based receiver that could acquire bistatic SAR signals from transmitters of opportunity such as ENVISAT and ERS-2; whereupon, in 2006, the RSLab at TSC-UPC initiated the project **SABRINA**: **SA**R **B**istatic **R**eceiver for **Interferometric A**pplications. The C-band version of this project, subsequently called SABRINA-C, was designed and fabricated; and since then, numerous successful acquisitions have been conducted. It has served as an experimental basis to study most aspects of bistatic SAR systems, including scattering phenomena, processing, hardware aspects linked to acquisition and synchronization etc. [8]; and at the same time, it has provided a means to perform bistatic SAR interferometry (across-track, along-track and differential), moving target indication (MTI) as well as tomography. Recently, polarimetric data, using RADARSAT-2 as the opportunity transmitter, has also been successfully acquired and processed.

After the launch of TerraSAR-X, it was proposed to develop the X-band version of SABRINA, which could use TerraSAR-X as a transmitter of opportunity. Compared to ENVISAT, ERS-2 and most other SAR missions, TerraSAR-X transmits a higher bandwidth and provides higher resolution. Therefore, performing bistatic imaging and interferometry or other SAR applications using TerraSAR-X signals would surely provide more detail, and hence a more rigorous analysis of bistatic processing issues can be performed. Following this aim, the X-band version of SABRINA has been recently designed at the RSLab, and is called **SABRINA-X**.

A detailed description of the hardware aspects of SABRINA-X is referred to [3]. As part of this thesis, the hardware aspects have been investigated in correspondence with acquisition of TerraSAR-X signals, and improved where necessary (or recommended for up-gradation/revision in future). The following sub-sections provide an overview of the system, and present the aspects that are critical for acquisition and subsequent processing.

2.2.1. System architecture

SABRINA-X is an X-band receiver that has been designed to operate at zero-IF (baseband), or a low-IF mode. It is a non-cooperative receiver i.e. it is not synchronized with the transmitter (which is space-borne, and the receiver is completely independent of it). Apart from the fact that there is no phase synchronization between the local oscillators of the receiver and the transmitter, there is also no synchronization between the transmission and the reception of the pulses; therefore, the PRF has to be estimated from the acquired signals.

SABRINA-X was initially designed with two input channels for reception; one receiving a direct signal from the transmitter while the other receives the signals backscattered by the viewed terrain. The direct signal is used to obtain the illumination envelope and PRF estimation.[1]

In order to perform interferometry, polarimetry or MTI, more channels are needed. A third channel has been recently integrated, and a fourth channel is under-construction. Figure 2.2.1 shows the architecture of the receiver, while the figure 2.2.2 shows the architecture of a single channel.

[1] The importance of the direct signal shall also be discussed in the chapter on range compression

Figure 2.2.1.: Sabrina-X receiver architecture

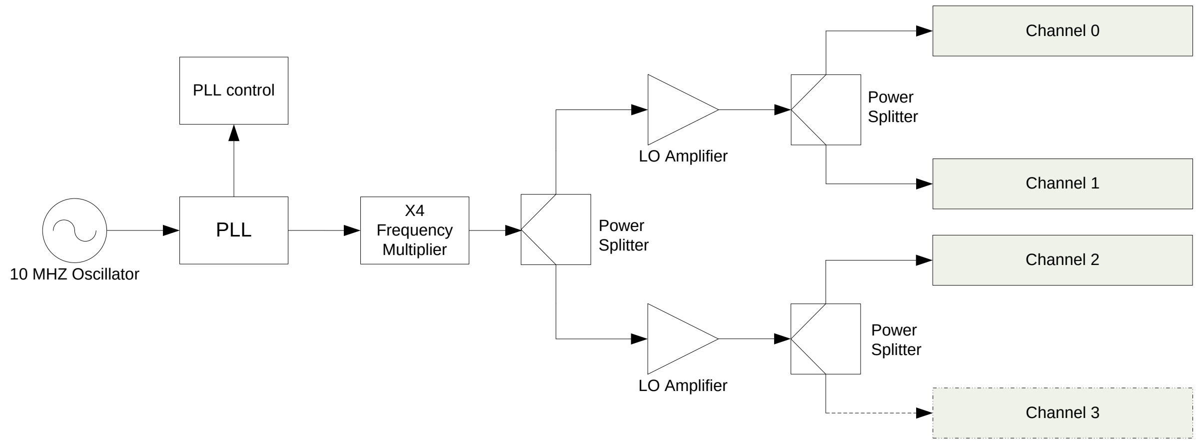

Figure 2.2.2.: Architecture of a single channel

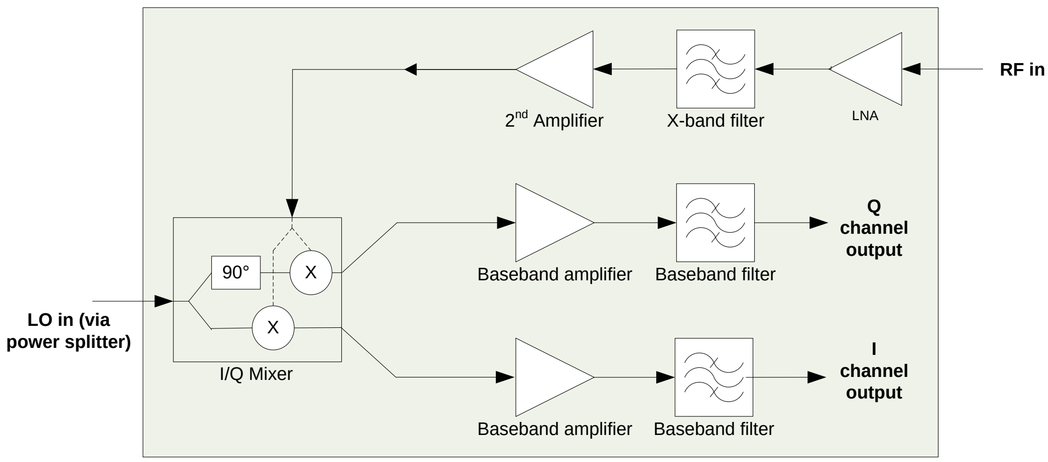

Figure 2.2.3.: RF circuitry (with power analysis for the direct signal acquisition)

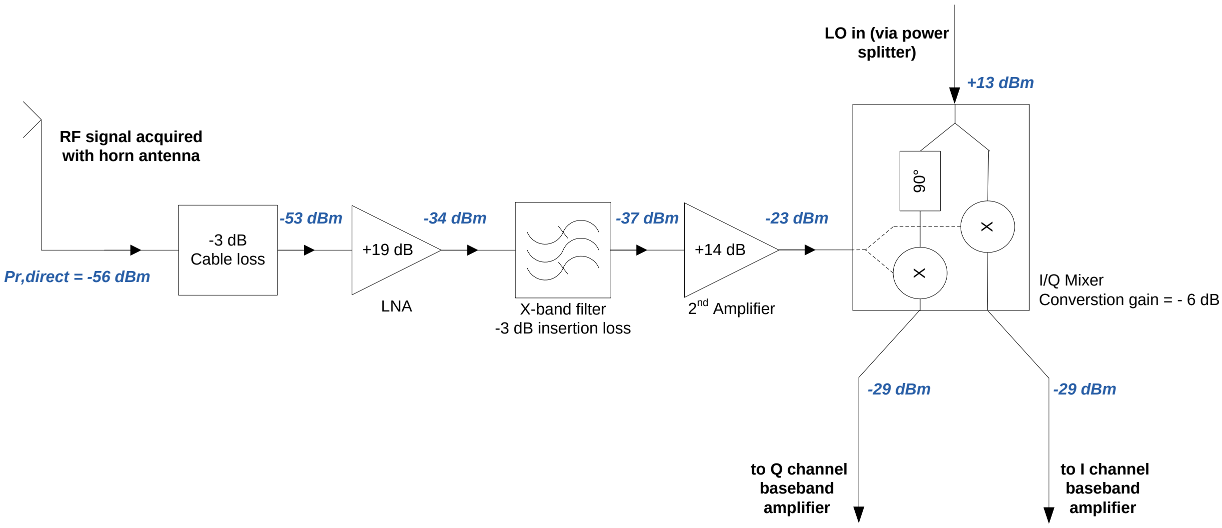

2.2.1.1. RF circuitry

The signals are acquired using pyramidal horn antennas, having a directivity of 18.2 dB. The antennas are connected to the receiver via low-loss cables (3 dB attenuation). Referring to [3]: From the antenna acquiring the direct signal from the satellite (orbiting at it's nominal orbital height), the approximate power received is

$$P_{r,direct} = -56.16 \text{ dBm}$$

and the power received by the antenna looking to the terrain falls within the following range (depending upon the reflectivity of the terrain)

$$P_{r,scattered} = -65.3 \text{ dBm (strong return)}$$

$$P_{r,scattered} = -86.5 \text{ dBm (weak return)}$$

The received signal, in each channel, is then amplified by a low-noise-amplifier (LNA), which has a gain of 19 dB in the band of interest (300 MHz bandwidth centered at 9.65 GHz). The LNA is housed in a tin-box, and a carbon fiber is stuffed under the box lids to prevent any spurious oscillation.

The amplified signal is then filtered by a bandpass filter (designed using coupled-lines over a grounded-plane). The pass-band extends from 9500 MHz to 9800 MHz, which is appropriate for the case of TerraSAR-X signals. Post-filtration, the signals are amplified again by a medium power amplifier (referred as the second RF amplifier). It provides a gain of 14 dB. The transmission lines at the input and the output of the amplifier chip (which is HMC4413LP3 manufactured by Hittite®) were previously based on microstrips. For improved performance (as recommended by [12]) in terms of any spurious self-oscillation, the layout has now been redesigned based on grounded coplanar waveguides.

Figure 2.2.4.: Local Oscillator (LO) and frequency synthesis, with typical power values

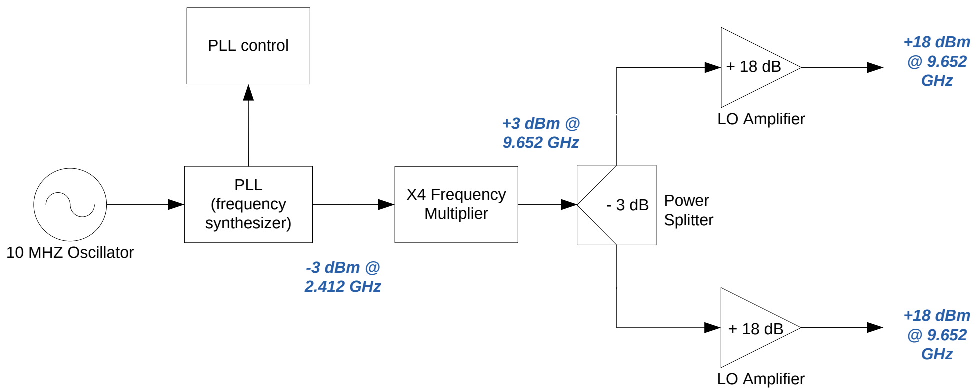

Afterwards, the signal is fed to an I/Q mixer (HMC521LC4), which generates two outputs; one is the in-phase(I) component and the other is the quadrature (Q) component. The input signal is mixed with the local oscillator (LO) frequency, downconverting it to a zero or non-zero IF frequency. The high-frequency products of mixing are filtered out, and only the low-frequency products appear at each I or Q output. At a LO drive is +13 dBm, the mixer's conversion gain is -6 dB. The I/Q outputs of the mixer are then fed to the baseband stage, discussed later.

Figure (2.2.3) shows the RF circuitry, with power analysis for the direct signal.

2.2.1.2. Local oscillator and frequency synthesis

The receiver uses a low-noise 10 MHz oscillator as the reference to synthesize the LO frequency. The oscillator has an excellent frequency stability (0.01 ppm over the temperature range of 0 - 70° C). A PLL based frequency synthesizer is programmed to synthesize the right frequency, $f_{\frac{1}{4}}$, which after getting multiplied by the x4 frequency multiplier, yields the desired LO frequency, f_{LO}.

For baseband operation (i.e. zero-IF), a LO frequency of 9.650 GHz is required. This implies that the desired frequency input to the x4 frequency multiplier is,

$$f_{\frac{1}{4},desired} = \frac{9650}{4} = 2412.5\,\mathrm{MHz}$$

However, the PLL used is not capable to generate the fractional 0.5 MHz (because it has a step size of 1 MHz). This implies that the step size of the LO frequency is

$$\nabla f_{LO} = 0.5 \times 4 = 2 \text{ MHz}$$

To acquire in baseband, the possible PLL and LO frequencies are shown in the table below:

PLL output frequency, $f_{\frac{1}{4}}$	*LO frequency, f_{LO}*
2412 MHz	9.648 GHz
2413 MHz	9.652 GHz

Keeping in view that the TerraSAR-X center frequency is 9.650 GHz, both the above options would lead to a spectrum shift of 2 MHz (i.e. the baseband spectrum would not be centered around zero frequency axis, as shown in the figure below.

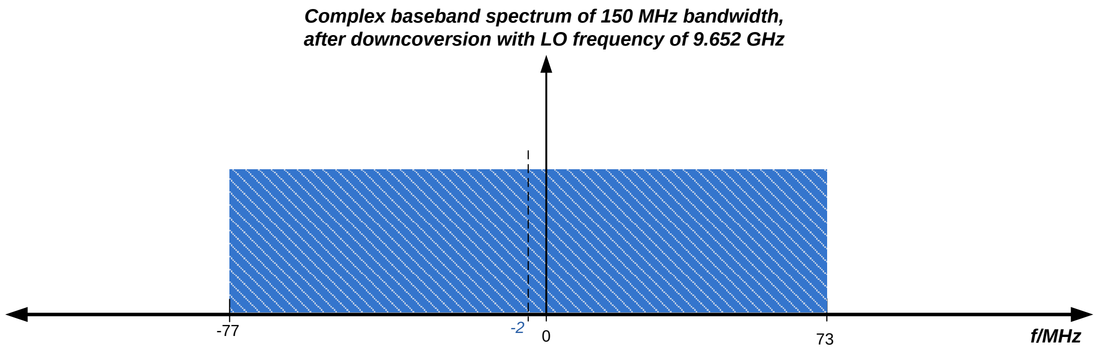

The LO frequency is later amplified, and split to feed individual receiver channels, as depicted in the figure 2.2.4.

2.2.1.3. Baseband circuitry and digitizer

The baseband circuitry is split in two branches, in each channel. The I output from the mixer enters one branch, while the Q enters the other. The two branches are essentially similar in design. In each branch, the input signal (I or Q) is fed to an amplifier, which provides a gain of 16.5 dB over the frequency range of DC to 1 GHz. The amplified signal is then filtered by a low-pass filter, with a 3-dB cut-off of 70 MHz, and 1-dB insertion loss in the pass-band.

The baseband filtration and the subsequent sampling has important implications regarding the acquisition of TerraSAR-X signals, as stated below:

- Since the filter has a cut-off of 70 MHz for both I/Q branch, theoretically only 140 MHz of transmit bandwidth is retained (whether the transmitted spectrum was 150 MHz or 300 MHz).

- The downconverted signals have to be sampled and recorded for processing. As per the Sampling Theorem, these signals (both I and Q) must be sampled with a sampling frequency, F_s greater than 140 MS/s.

- The digitizers currently available in the RSLab are PXI-5124 National instruments acquisition cards. They have the following specifications:

- 2 channel simultaneous sampling
- 12 bit resolution
- Sampling at up to 200 million samples per second (MS/s), or 100 MS/s and below
- 512 MB of memory channel (256 million samples)
- Due to some limitations of the temporal window of opportunity[2], we may have to use a sampling frequency of $F_s = 100\ \mathrm{MS/s}$, instead of 200 MS/s. (Refer to section 3.2.1.2 for details on the window of opportunity)

• As per the Shannon's sampling theorem, sampling the I/Q baseband signals at 100 MS/s would allow retention of only 100 MHz of (complex) bandwidth.

• However, since the filters have 70 MHz cut-off, frequency components above 50 MHz in both I and Q branches would be aliased during the sampling. Hence, we would require additional baseband filtration, to prevent aliasing.

• To ensure that the sampled signals are alias-free we have, therefore, incorporated a pre-sampling additional low-pass filter having a 3-dB cut-off at 48.5 MHz and 1-dB insertion loss in the pass-band, as shown below:

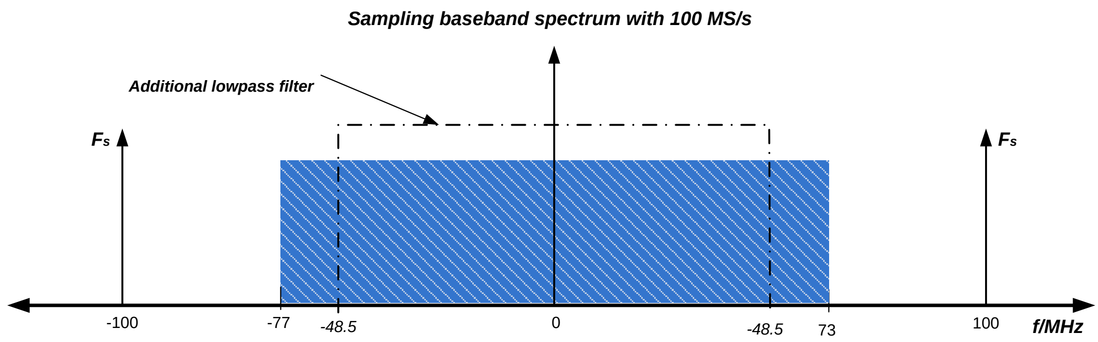

The baseband circuitry is depicted in the figure 2.2.5.

2.2.2. Acquisition modes: IF/IQ

Keeping in view the hardware considerations and limitations mentioned previously, this sub-section pictorially represents the steps in the I/Q acquisition and a possible low-IF acquisition mode.

[2]The signals have to be acquired at the time when the satellite is passing over the terrain, and illuminating it. The wider the temporal window of acquisition, the more the chances of not missing the satellite illumination. Choosing a higher sampling rate reduces the window, as the digitizer memory is consumed in shorted time.

Figure 2.2.5.: Baseband circuitry, with typical power values for the case of direct signal acquisition

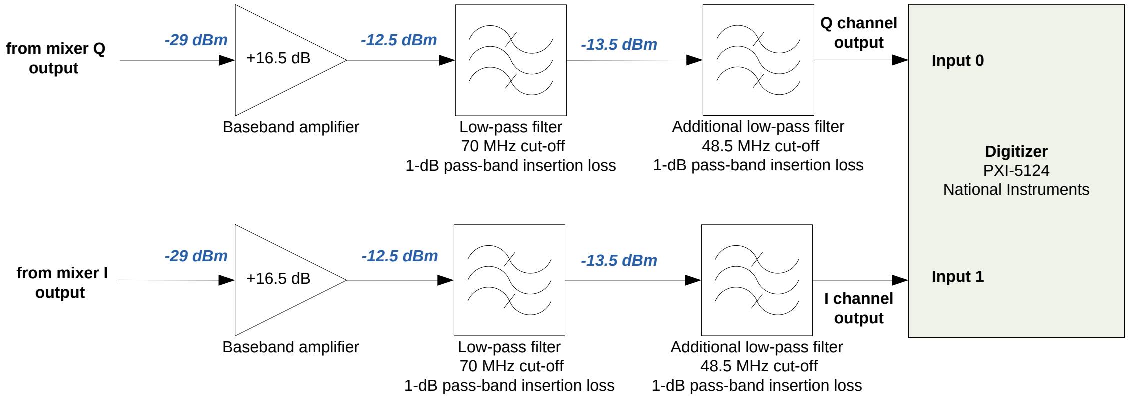

2.2.2.1. I/Q Acquisition mode

Figure 2.2.6 shows the I/Q acquisition mode. This mode has the following characteristics:

- LO frequency of 9.652 GHz
- If the sampling frequency, $F_s = 100\ \mathrm{MS/s}$ is used, then we need the additional 48.5 MHz cut-off low-pass filters in each I and Q branch after downconversion. The corresponding bandwidth retained is, $B_{pulse} = 97\ \mathrm{MHz}$
- If the sampling frequency, $F_s = 200\ \mathrm{MS/s}$ is used, then we do not need the additional 48.5 MHz cut-off low-pass filters; instead the 70 MHz cut-off low-pass filters would suffice. The corresponding bandwidth retained is, $B_{pulse} = 140\ \mathrm{MHz}$.

2.2.2.2. Low-IF Acquisition mode

Figure 2.2.7 shows the low-IF acquisition mode. This mode has the following characteristics:

- LO frequency of 9.7282 GHz
- If the sampling frequency, $F_s = 100\ \mathrm{MS/s}$ is used, then we need the additional 48.5 MHz cut-off low-pass filters in each I or Q branch after downconversion. In IF operation, we need to use either I or Q branch in each channel, and not both. The corresponding bandwidth retained is, $B_{pulse} = 48.5\ \mathrm{MHz}$.
- If the sampling frequency, $F_s = 200\ \mathrm{MS/s}$ is used, then we do not need the additional 48.5 MHz cut-off low-pass filters; instead we need low-pass filters with a cut-off of below 100 MHz (to be designed in future). The corresponding bandwidth retained is, $B_{pulse} = 100\ \mathrm{MHz}$.

Figure 2.2.6.: I/Q (zero-IF) Acquisition

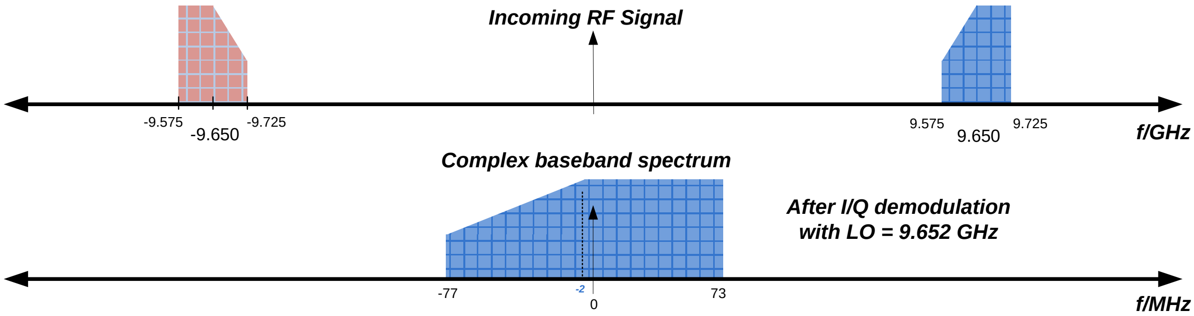

(a) Downconversion with $f_{LO} = 9.728$ GHz

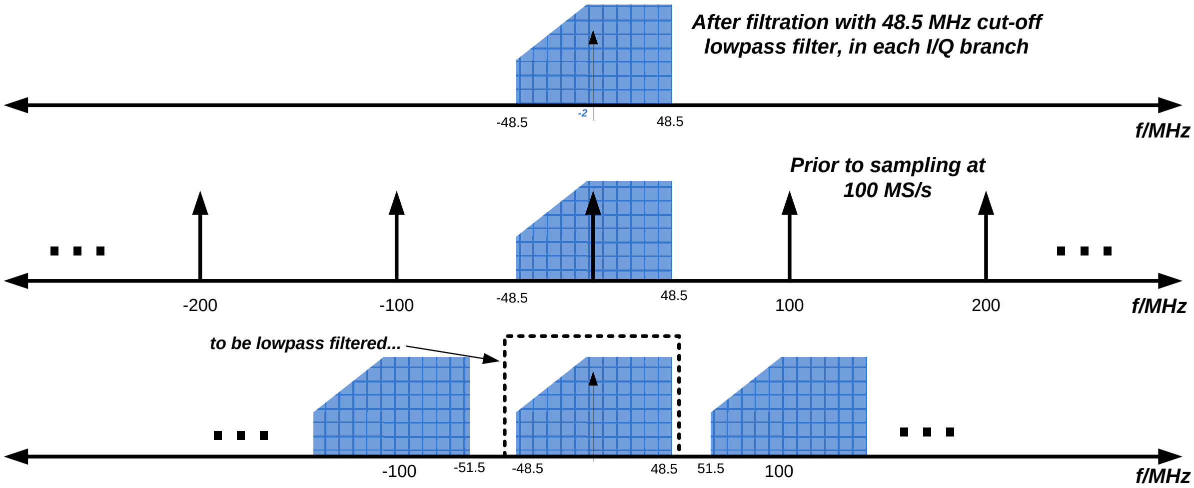

(b) Filtration and sampling at $F_s = 100\ \mathrm{MS/s}$

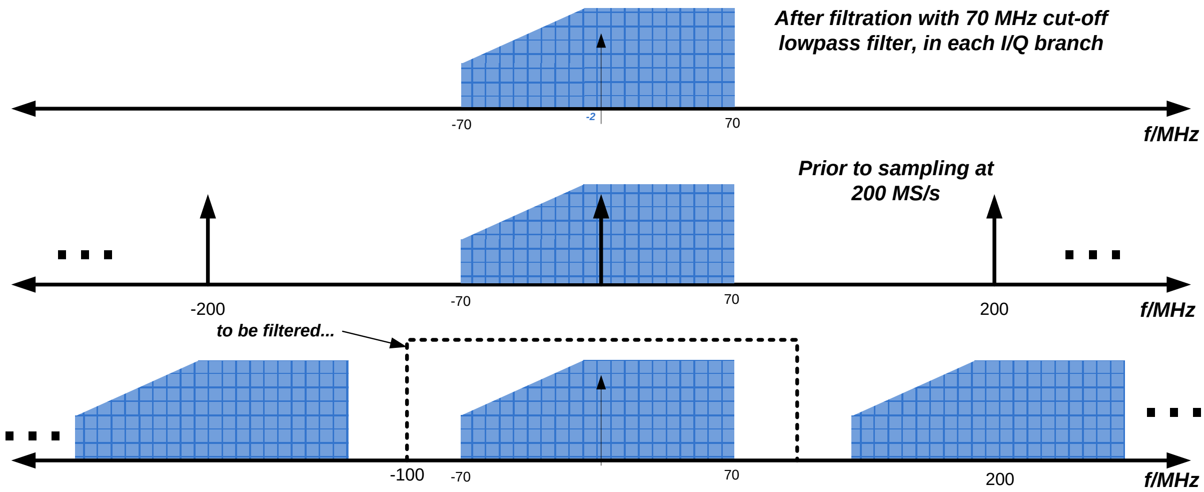

(c) Filtration and sampling at $F_s = 200\ \mathrm{MS/s}$

Figure 2.2.7.: Low-IF Acquisition

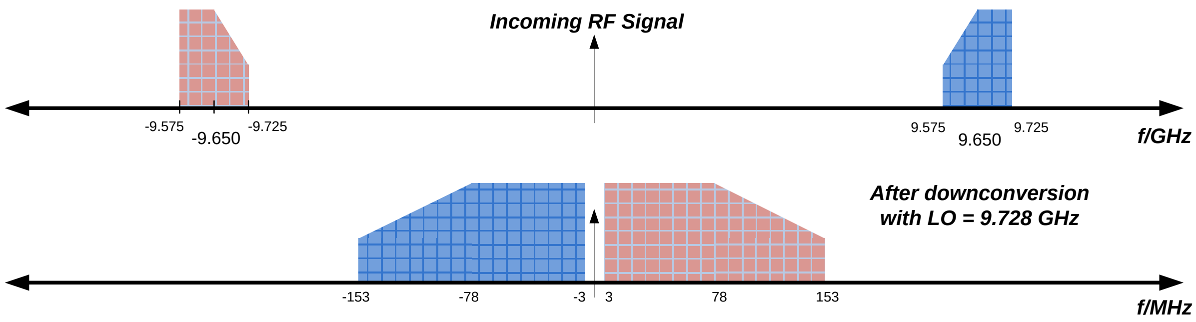

(a) Downconversion with $f_{LO} = 9.728$ GHz

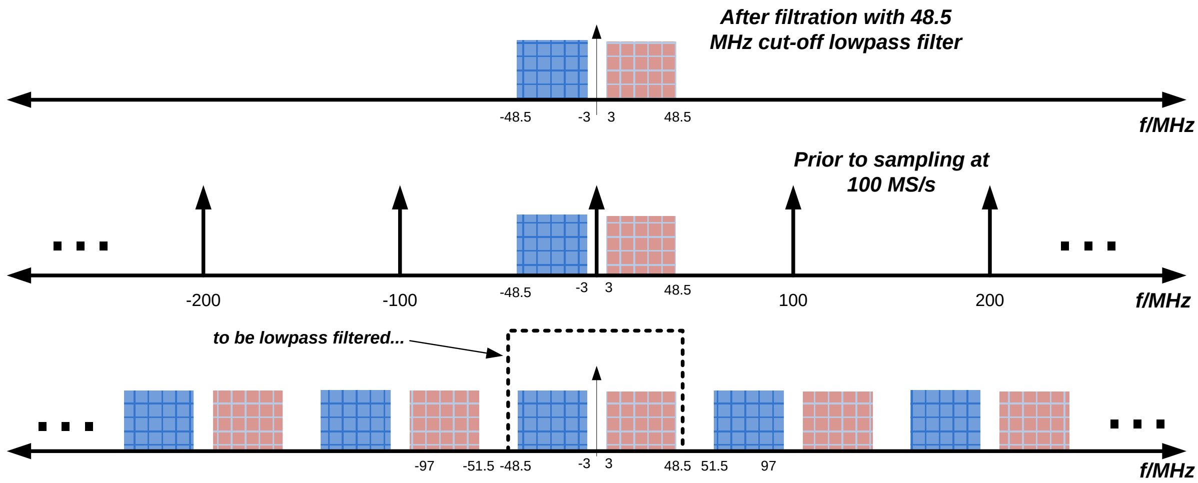

(b) Filtration and sampling at $F_s = 100\ \mathrm{MS/s}$

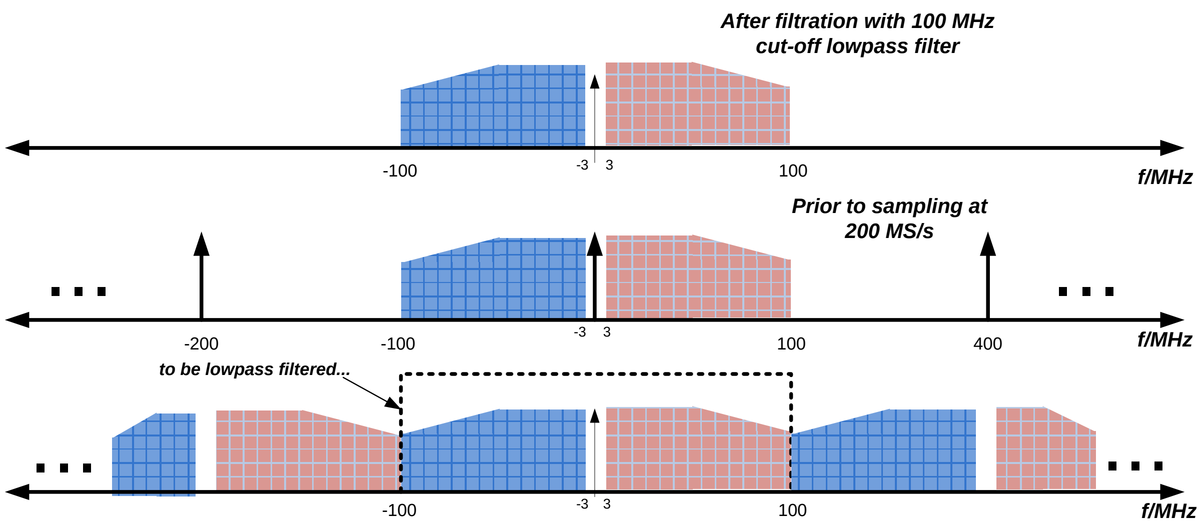

(c) Filtration and sampling at $F_s = 200\ \mathrm{MS/s}$

Figure 2.2.8.: Channel frequency responses: Baseband signals I(Cyan)/Q(Blue)

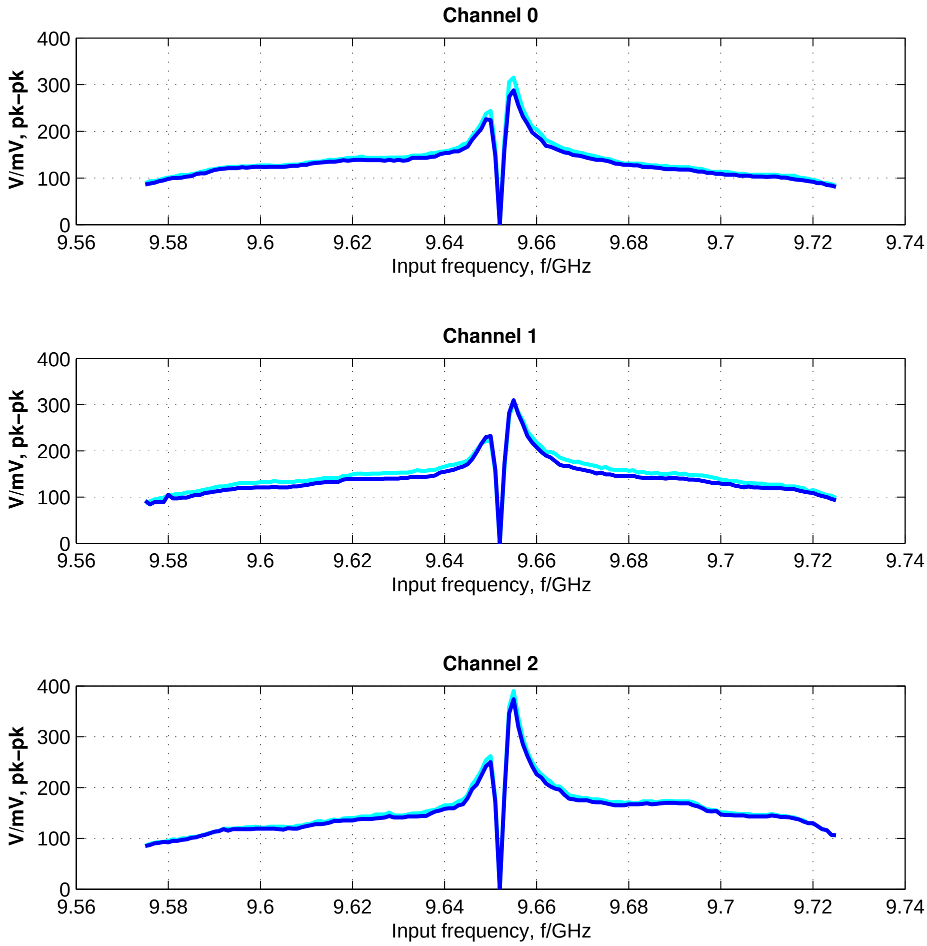

2.2.3. Channel frequency response

This section delineates the frequency response of the channels. For each of the three channels (channel 0,1 and 2), a frequency sweep from 9.575 to 9.725 GHz is applied at the RF inputs, having a power level of -54 dBm. The LO frequency is kept at 9.652 GHz. The results are shown in the figure 2.2.8.

The null at 9.652 GHz is expected, since mixing it with the LO frequency, $f_{LO} = 9.652$ GHz leads to a DC value which is being blocked by the subsequent baseband amplifier (amplifying it would imply amplifying noise).

2.2.3.1. Gain and resonance effects

The channel gain curves are given in figure 2.2.9; it can be noted that the channel gains remain around 40 dB in the frequency band of interest (9.575 to 9.725 GHz). The channel gains are

Figure 2.2.9.: Channel gain: Baseband signals I(Cyan)/Q(Blue)

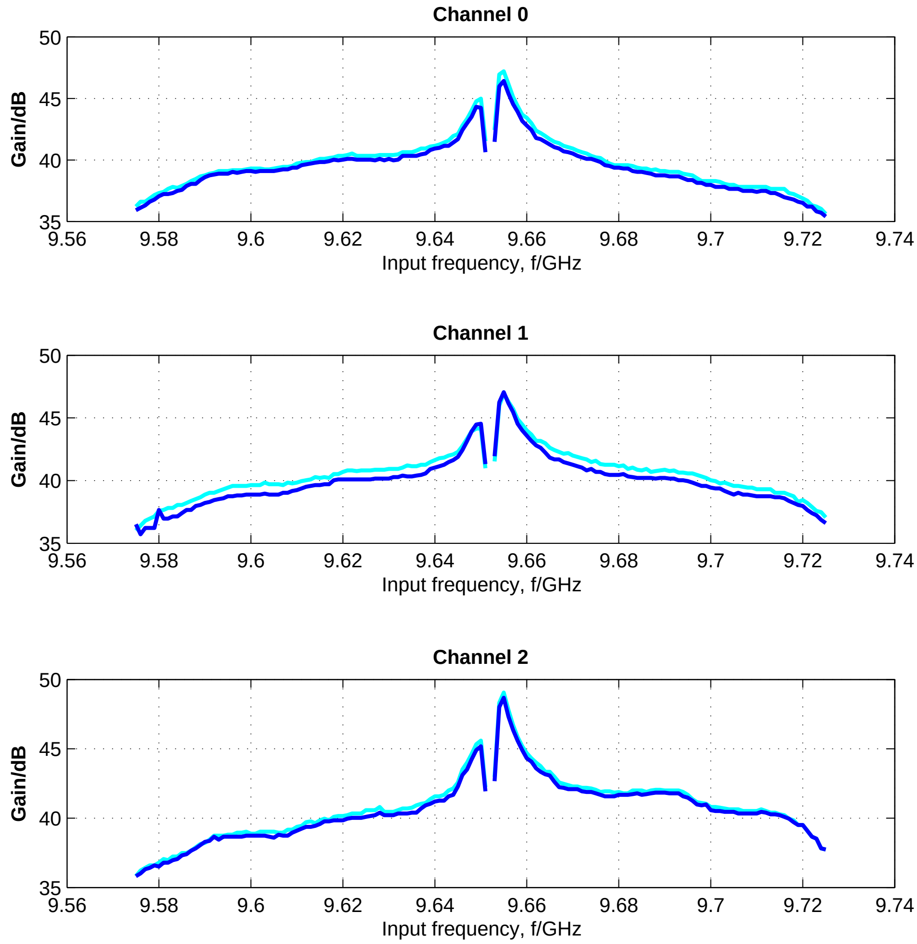

not identical from one channel to the other, although not too distinct either. It suggests that we may expect slightly different power levels in the subsequently processed (compressed/focused) SAR images from each channel. Apart from that, it is also noticeable that:

1. There are resonance peaks on both sides of the frequency 9.652 GHz, in each I and Q branch, which are unexpected.

2. The resonance is slightly more on the right side than the left

3. Resonance peak falls at 9.655 GHz and 9.6495 GHz, as shown in the figure below

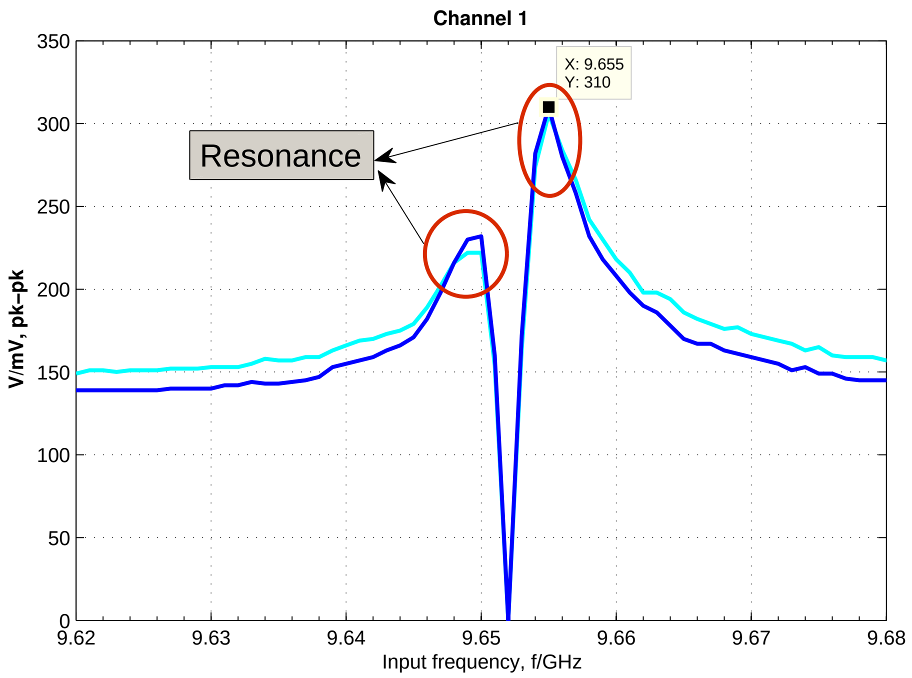

These resonances are unwanted; and in fact, as discussed in the subsequent chapters on processing, these resonances badly tamper range processing. Future improvement of the system must attempt to find a way to remove them. As part of this thesis, attempts are made to compensate them during the processing stage.

3. Acquisition Campaigns

This thesis presents two successful bistatic SAR data acquisitions, with SABRINA-X receiver and using TerraSAR-X as the opportunity transmitter. This chapter entails the campaign activities necessary for a successful acquisition.

As stated in 2.1.1, TerraSAR-X has a repeat period of 11 days. It implies that theoretically the acquisitions can be repeated after 11 days; however, the transmission of signals from the satellite is a propriety of DLR (the German Aerospace Center), and generally the transmission has to be requested and even paid for.

The first acquisition (subsequently referred to as 'Acquisition 1') was performed on April 03, 2010. The transmission characteristics known in advance were:

- Stripmap mode of transmission
- Transmitted bandwidth: 150 MHz at center frequency of 9.650 GHz
- Right-looking transmission

The other important characteristics, such as the pulse length, pulse repetition frequency (PRF), chirp-rate etc., have to be estimated from the acquired data (referred to section 4.3.3).

The second acquisition (subsequently referred to as 'Acquisition 2') was performed on June 02, 2010. The transmission characteristics known in advance were:

- (Sliding) Spotlight mode of transmission
- Transmitted bandwidth: 80 MHz at center frequency of 9.650 GHz
- Right-looking transmission

As for the Acquisition 1, the other important transmission characteristics have to be estimated from the acquired data.

3.1. Scenario

3.1.1. Viewed scene

Figure 3.1.1 shows the scenery being viewed, which is a view of the Barcelona harbor. The intention in selecting this scene is the fact that it has a wide range of targets, such as the metal silos and ship (which tend to reflect strongly), calm water (which tends to reflect very weakly) etc. In the processed images, we would expect to identify the targets accordingly.

Figure 3.1.1.: Viewed terrain: Strong back-scatterers (such as the ship and metal silos) and weak back-scatterers (such as calm sea)

3.1.2. Back-scattering geometry

The satellite transmission, for both Acquisition 1 and 2, is right-looking. The scene as shown in the figure above, is viewed from the side of mountain, such that both the transmitter (satellite illumination) and the receiver are on one side of the terrain. This corresponds to a back-scattering geometry, as shown in the figure 3.1.2. The receiver set-up has an altitude of 126 m above sea level.

Figure 3.1.2.: Back-scattering geometry, with right-looking satellite transmission

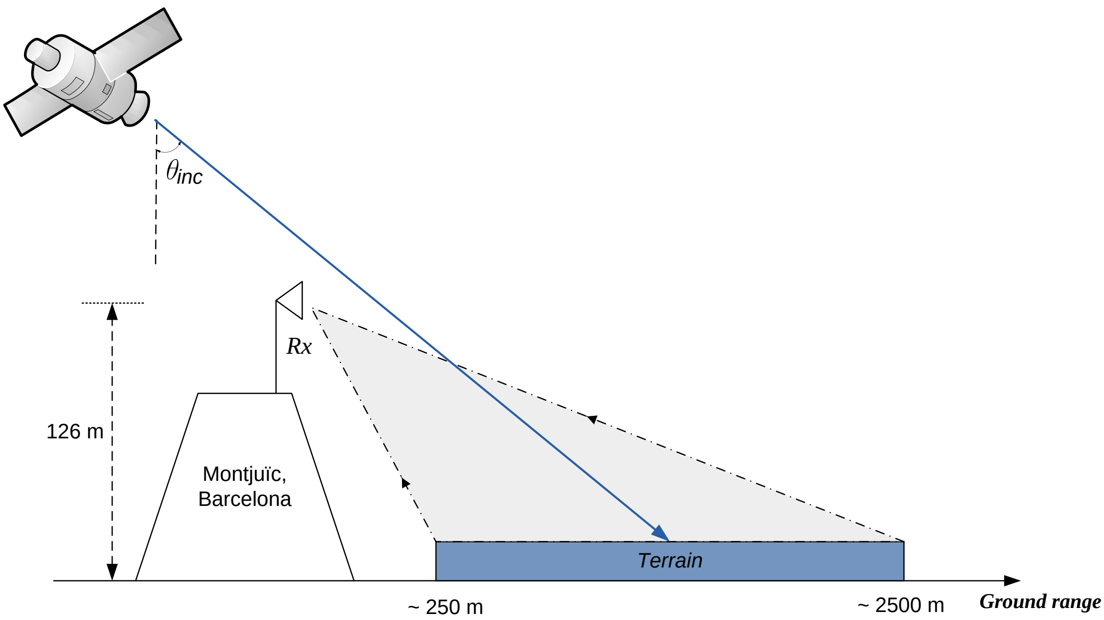

3.2. Experimental set-up

3.2.1. Satellite pass

3.2.1.1. Two-line Keplerian-elements (TLE)

Prior to acquisition, it is imperative to predict the satellite overpass time i.e. the time when the satellite is closest in range to the location of the receiver set-up. This time corresponds to the zero-Doppler time (ZDT) instant as well. It is calculated using the simplified general perturbations version 4 (SGP4) orbit propagation algorithm [13], which is implicitly employed by using the two-line Keplerian-elements (TLE) set. TLE sets are available from a number of on-line sources such as `http://www.celestrak.com/`.

A TLE set contains orbital elements that describe the orbit of an earth satellite. There are numerous free, open-source programs that can compute the precise position of a satellite at a particular time using the TLE set, such as the GNOME Predict[1]. However, prior to Acquisition 1 and 2, the software used to predict the satellite position and overpass time is the one that has been developed at the RSLab, and it has provided reliable computations for the numerous acquisitions performed with SABRINA-C with ENVISAT, ERS-2 and RADARSAT-2 as the opportunity transmitters, such as in [2], [14]. It requires the location of the receiver set-up and its altitude above ground as input, which are (41.366701° N, 2.169263° E) and 126 m. The error in the prediction of the overpass time has been found to be less than 0.5 seconds [14].

The TLE set used for Acquisition 1 is:

```
1 31698U 07026A 10093.02048584 .00000142 00000-0 99675-5 0 1211
2 31698 97.4453 101.2836 0001609 85.0246 359.7814 15.19152877155276
```

and the TLE set used for Acquisition 2 is:

```
1 31698U 07026A 10153.22008222 .00000369 00000-0 20780-4 0 3049
2 31698 97.4432 160.6274 0001613 81.7854 341.0297 15.19152637164410
```

These TLE sets are in the standard format. Details of the physical meaning associated with these numbers can be referred to [15].

Figure 3.2.1 shows the time variation of the distance of the satellite from the receiver, indicating the ZDT as the instant when the distance is closest to the receiver (shown as the instant when time is 0 seconds). The corresponding UTC time is shown in the table below:

Acquisition	ZDT (UTC Time)	Distance corresponding to ZDT
1 (April 03, 2010)	17:41:20.315	619580.7 m
2 (June 02, 2010)	17:49:55.884	739050.6 m

[1] GNOME Predict is an open-source, Linux package available at: `http://directory.fsf.org/project/gpredict/`

Figure 3.2.1.: Prediction of the time variation of the distance between the satellite and the receiver

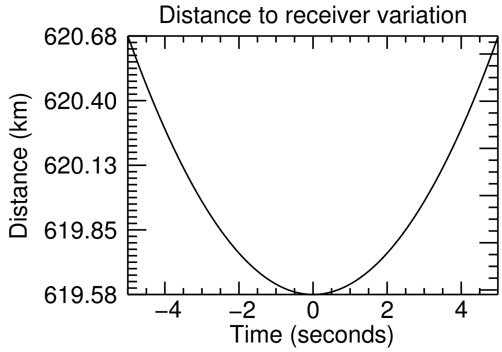

(a) Acquisition 1

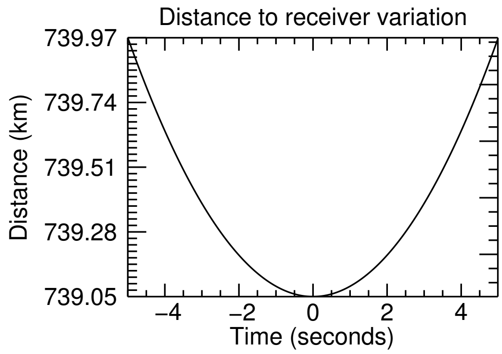

(b) Acquisition 2

3.2.1.2. Temporal window for acquisition

SABRINA-X is a non-cooperative receiver, which implies that there is no synchronization between the transmitting satellite and the receiver on ground. Therefore, apart from a lack of phase synchronization, the moments of incidence of the incoming pulses is also unknown. This necessitates that the received signals, after downconversion, have to be sampled continuously. Since the memory of the digitizers is limited (512 MB per channel, corresponding to 256 million samples with 12-bit resolution), the duration of the signals acquired and sampled is limited.

With sampling frequency, $F_s = 100\ \mathrm{MS/s}$, the duration of the sampled signal (which is equivalent to the window of acquisition) is,

$$T_{100} = \frac{256 \times 10^6}{100} = 2.56\ \mathrm{seconds} \tag{3.2.1}$$

and with $F_s = 200$ MS/s,

$$T_{200} = \frac{256 \times 10^6}{200} = 1.28 \text{ seconds}$$

A duration of 1.28 seconds may not be sufficient to ensure a successful acquisition of the main-lobe of the satellite transmission, keeping in view the fact that the prediction of ZDT as per the last section may have an error of 0.5 seconds. Therefore, we used a sampling frequency of $F_s = 100$ MS/s, instead of 200 MS/s for both Acquisition 1 and 2. The following table summarizes:

Acquisition	Sampling frequency, F_s	Window of acquisition
1 (April 03, 2010)	100 MS/s	2.56 seconds
2 (June 02, 2010)	100 MS/s	2.56 seconds

3.2.2. Antenna orientations

For a successful acquisition, it is imperative to correctly orient the antennas used to receive the signals, especially the antenna used to acquire the direct signal from the satellite transmitter. It is the absence of a dedicated link between the transmitter and the receiver local oscillators that necessitate the use of the direct signal for PRF recovery and phase synchronization [16]. The direct signal can be acquired as

1. a dedicated channel input to the receiver, with an antenna pointing directly to the satellite;
2. else, it may be received via the side-lobes of the antenna viewing the terrain [2].
3. Another option is using two antennas with one pointing directly to the satellite while the other looks to the terrain, and combine the two with a hardware coupler/combiner prior to input into the same receiver channel.

It needs to be emphasized that currently there are only 2 digitizer cards (i.e. 4 inputs prior to sampling) available in the RSLab. This is one of the bottlenecks, as it limits the acquisition to only two channels (each with one I and one Q branch).

For the Acquisition 1, the intention was to perform bistatic interferometry besides imaging. In order to obtain an interferogram, two complex images are required, which asks for two channels acquiring the scattered signals from the viewed terrain. Keeping in view the above-mentioned bottleneck, there is no possibility of acquiring a dedicated direct signal from the satellite as both the two channels are acquiring the scattered signals. In this situation, the direct signal was acquired by using option 3 above. For Acquisition 2, the intention was imaging only; therefore, the direct signal was acquired with option 1.

Regardless, in both the acquisitions, the antenna pointing to the satellite needs to be correctly oriented to receive the direct signal. As for the prediction of the satellite position and ZDT, there are free, open-source software that can provide the azimuth and the elevation angles required; however, we used the software already developed in RSLab for the purpose, appreciating the fact that it has provided reliable computation for the numerous acquisitions already conducted with SABRINA-C receiver (such as in [2]).

Figure (3.2.2) shows the antennas configuration for Acquisition 1. Two antennas look to the scene with a vertical separation i.e. baseline B_v of 112 cm, while one antenna captures the direct signal. For acquisition 2, only one antenna looked to the scene, while the other received the direct signal.

The following table summarizes:

Acquisition	Direct signal acquisition	θ_{inc}	θ_{az}	θ_{el}
1 (April 03, 2010)	combined with scattered (option 3)	35.5°	260.3° (NE)	54.5°
2 (June 02, 2010)	dedicated acquisition (option 1)	48.3°	258.7° (NE)	41.7°

Figure 3.2.2.: Direct and scattered channel antennas configuration

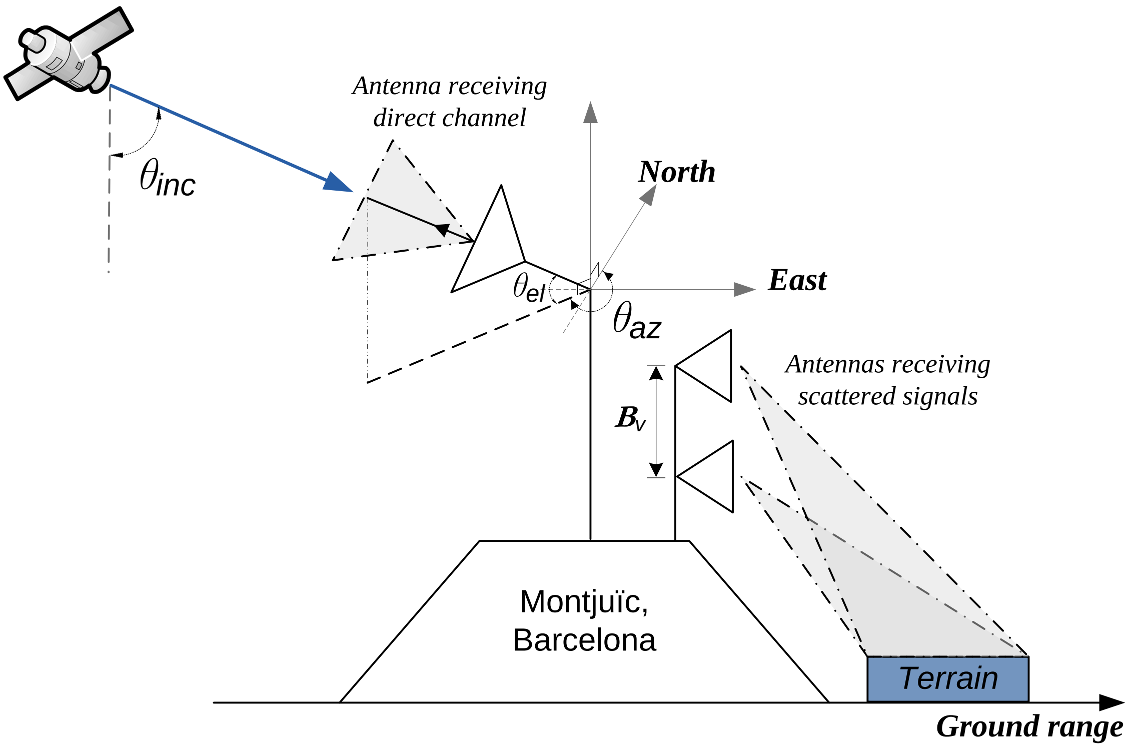

Figure 3.2.3.: Acquisition campaign 1

(a) Direct and scattered channel antennas configuration

(b) SABRINA-X

4. Pre-processing

This chapter briefly entails the first steps towards the processing of the acquired data signals, as per the experimental set-up discussed in the last chapter. The characteristics of the signals, such as the pulse duration, chirp-rate and pulse-repetition-frequency (PRF) have to be estimated from the data, as there are not known in advance. Moreover, we have to quantitatively analyze any aliasing and filter the received signals respectively.

The details of the pre-processing steps are not discussed here, since the algorithms used for that have already been devised over the last few years at the RSLab and are not a part of this thesis work. These details are referred to [14, 16, 17]. The following sections tend to highlight the application of these steps on the signals acquired in April and June acquisition campaigns.

4.1. Pulse trains

The satellite transmits pulsed chirp signals. Therefore, the acquired signals are pulse trains, as shown in the figure 4.1.1, which is a small extract of the entire pulse train recorded over the window of acquisition. The sudden spikes in the pulses owe to the resonance introduced by the hardware.

Figure 4.1.1.: Acquired pulse train: Acquisition 2, Direct signal

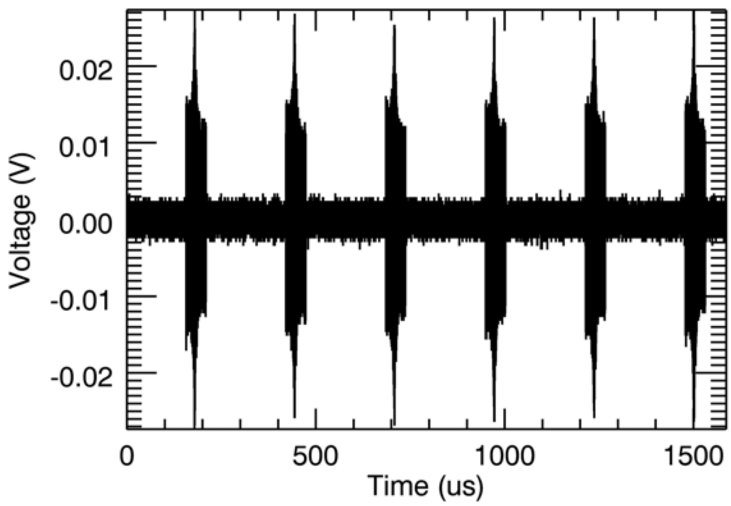

Figure 4.2.1.: Illumination Envelopes: Acquisition 1 (April 03, 2010: Stripmap)

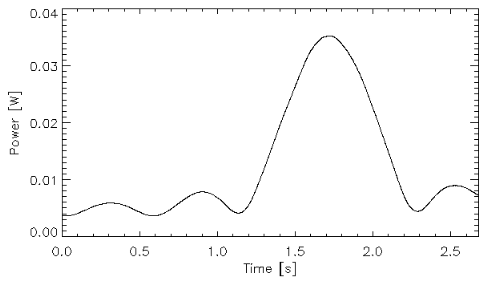

(a) Direct + Scattered Signal: Branch I

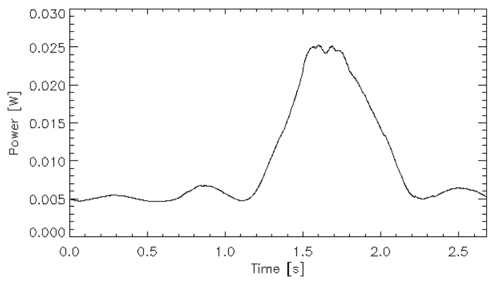

(c) Scattered Signal: Branch I

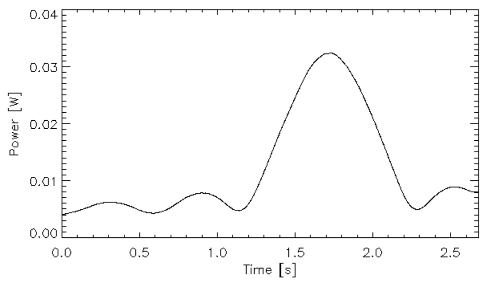

(b) Direct + Scattered Signal: Branch Q

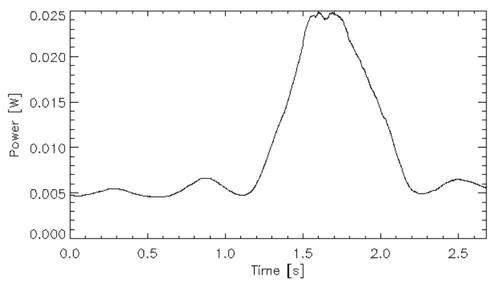

(d) Scattered Signal: Branch Q

4.2. Illumination envelopes

As a first step after the acquisition of signals, we need to make sure whether the main-lobe of the illumination has been acquired. It is the main-lobe signals (being significantly higher in power than the side-lobes) that are used for subsequent processing towards imaging and interferometry.

The figure 4.2.1 shows the power envelopes of I/Q acquired signals for the Acquisition 1. The power envelope is obtained by taking the peak of the absolute power in each pulse, and plotting the evolution of the peaks [17]. The 'Direct + Scattered' envelopes correspond to the combined acquisition of the signal received directly from the satellite and the signal backscattered by the terrain. The reason for the combined acquisition is as discussed in 3.2.2.

Figure 4.2.1 shows the envelopes for the Acquisition 1. The shape of the acquired envelopes correspond to the amplitude modulation introduced by the antenna radiation pattern. It is noticeable that the main-lobe is not centered in the middle of the acquisition window, which implies an error in the prediction of the satellite overpass time. The window of acquisition is 2.56 seconds (because the sampling frequency has been 100 MS/s, refer to equation 3.2.1 for the calculation). The peak of the main-lobe, for acquisition 1, falls at

$$t_{main\,lobe,1} = 1.75605 \text{ seconds}$$

Figure 4.2.2.: Illumination Envelopes: Acquisition 2 (June 02, 2010: Sliding spotlight)

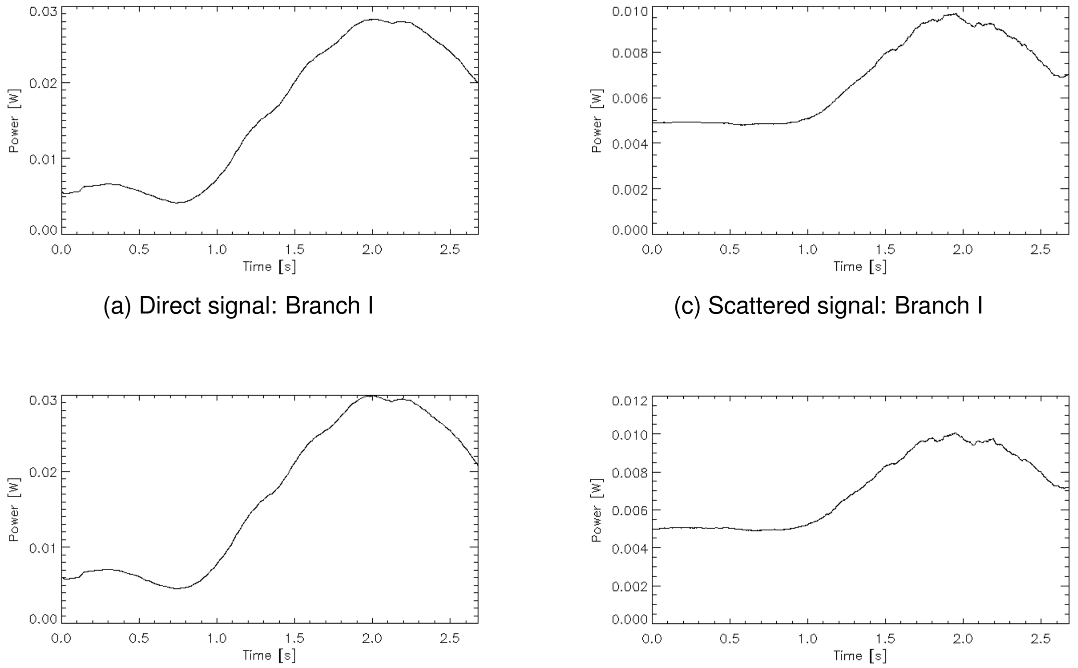

(a) Direct signal: Branch I

(c) Scattered signal: Branch I

(b) Direct signal: Branch Q

(d) Scattered signal: Branch Q

and the corresponding error is

$$e_1 = \frac{2.56}{2} - 1.75605 = -0.37605 \text{ seconds}$$

The main-lobe of radiation for the stripmap mode extends over around 1.2 seconds. It is of significance to mention here that if the sampling frequency would have been $F_s = 200$ MS/s leading to an acquisition window of 1.8 seconds, it would have been risky to capture the entire main-lobe keeping into consideration the prediction error computed above.

The power envelope for Acquisition 2 in figure 4.2.2 does not correspond to the radiation pattern of the transmit antenna, because the transmission is in the sliding spotlight mode whereby the antenna steers the radiation pattern to focus the viewed terrain with prolonged illumination. Due to this prolonged illumination, main-lobe of the acquired signals is longer than the stripmap case. However, as for Acquisition 1, it is off-center. The peak of the main-lobe falls at

$$t_{main\,lobe,2} = 2.03057 \text{ seconds}$$

and the corresponding error is

$$e_2 = \frac{2.56}{2} - 2.03057 = -0.75057 \text{ seconds}$$

Figure 4.3.1.: A zoomed look at the acquired chirp signals in time (S_I in purple, S_Q in blue and $|S|$ in black): Direct signal, Acquisition 2

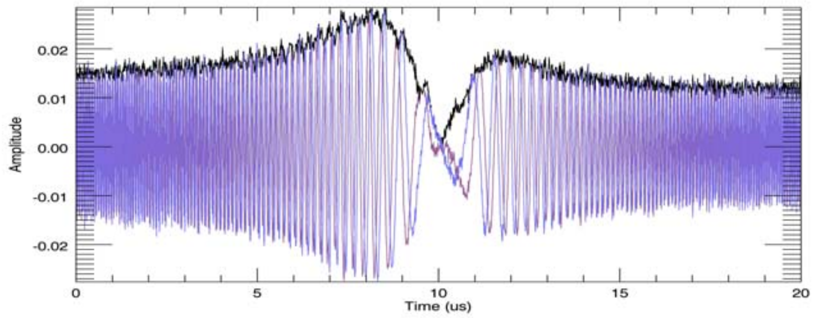

4.3. Chirp Analysis

Analyzing the received chirp signals is of prime importance. The in-phase acquired data (from branch I), S_I and the quadrature-phase data (from branch Q), S_Q, are combined to give the baseband signal,

$$S = S_I + j \cdot S_Q \tag{4.3.1}$$

Figure 4.3.1 shows the I/Q data and the complex sum as above. It shows the temporal evolution of the chirp signal, emphasizing the changing frequency with time i.e. (frequency modulation) and that the I and Q signals traverse in quadrature phase difference to each other.

4.3.1. Anti-alias filtration

Figure 4.3.2 shows the chirp signals in time, their frequency spectrum and spectrograms for Acquisition 1. From the spectrogram of the direct + scattered signal, in figure 4.3.3c, it can be noticed that there is some aliasing, for frequency components above 50 MHz, though the acquisition was done with the additional 48.5 MHz cut-off low-pass filters in the baseband circuity. The aliasing appears as the 'fold' or 'flip' in the slope of the chirp, around the $\pm$50 MHz frequency. It occurs due to the fact that the filters do not have a very sharp transition from pass-band to stop-band, as would be desired ideally. After removing aliasing, only 80 MHz of bandwidth is retained.

The scattered signal shows more aliasing, because it was acquired without the additional 48.5 MHz cut-off filters[1]. After removing aliasing, only 40 MHz of bandwidth is retained.

The alias-free signals for Acquisition 1 are shown in figure 4.3.4. For Acquisition 2, as is noticeable from figure 4.3.4c and figure 4.3.4f, there is no aliasing. This owes to the fact that the satellite transmission was limited to 80 MHz bandwidth as opposed to the case of Acquisition 1 when the transmit bandwidth was 150 MHz.

[1]Only a limited number of these filters could be readied till the day of the acquisition campaign; therefore, the scattered channel had to be acquired without them.

Figure 4.3.2.: Acquired chirp signals in time, their frequency spectrum and spectrograms: Acquisition 1

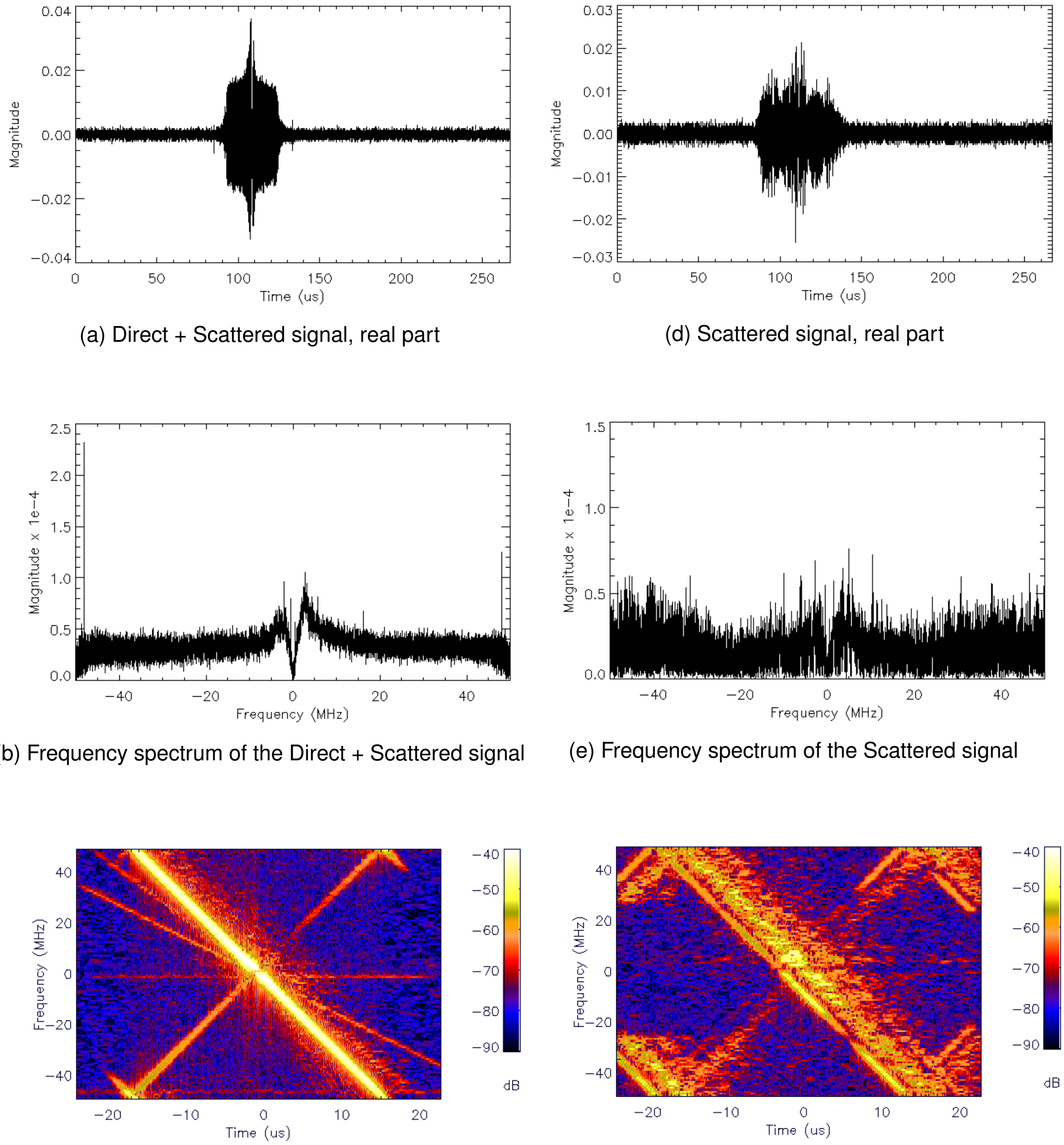

(a) Direct + Scattered signal, real part

(d) Scattered signal, real part

(b) Frequency spectrum of the Direct + Scattered signal

(e) Frequency spectrum of the Scattered signal

(c) Spectrogram of the Direct + Scattered signal

(f) Spectrogram of the Scattered signal

Figure 4.3.3.: Acquired chirp signals in time, their frequency spectrum and spectrograms: Acquisition 2

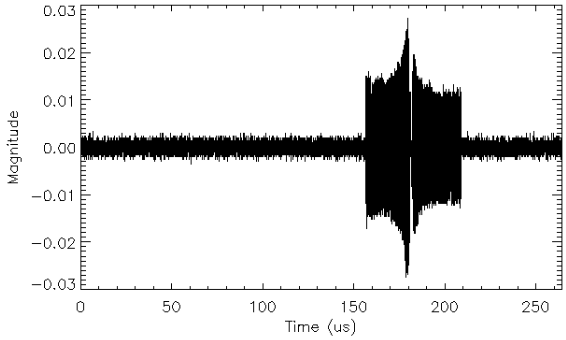

(a) Direct signal, real part

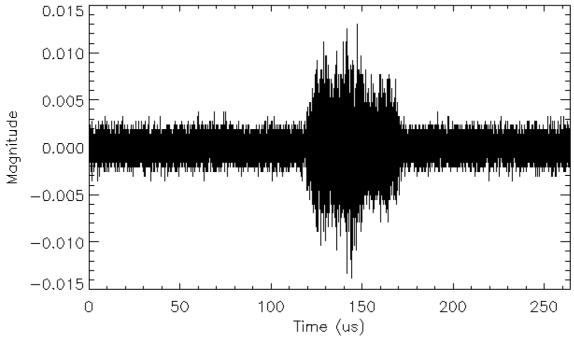

(d) Scattered signal, real part

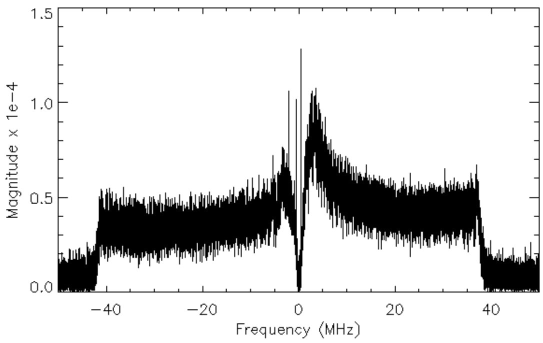

(b) Frequency spectrum of the Direct signal

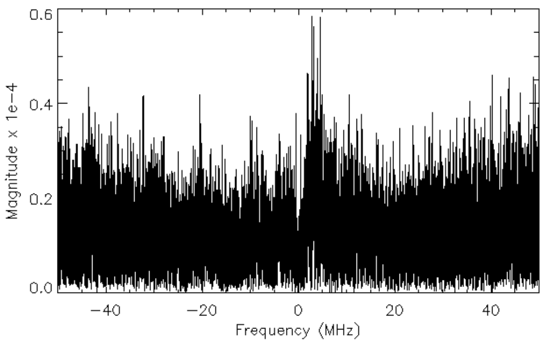

(e) Frequency spectrum of the Scattered signal

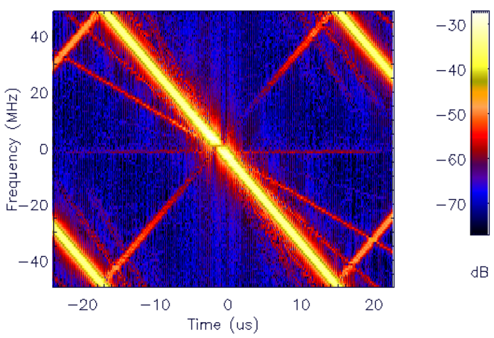

(c) Spectrogram of the Direct signal

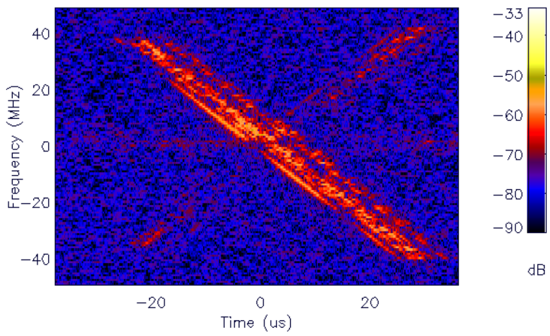

(f) Spectrogram of the Scattered signal

Figure 4.3.4.: Spectrograms after anti-alias filtration: Acquisition 1

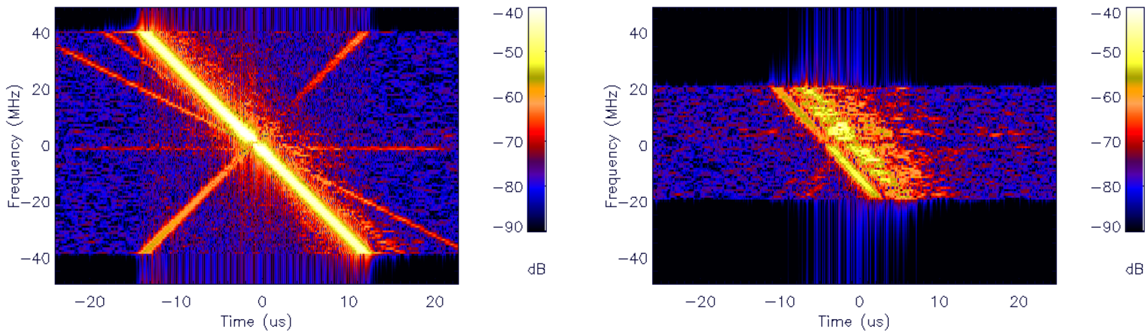

(a) Direct + Scattered signal after anti-alias filtration

(b) Scattered signal after anti-alias filtration

4.3.2. 'Off-nominal' Transmissions

An important observation regarding the acquired signals is the fact that the satellite is not transmitting a single linear chirp, as would nominally be expected. Apart from one strong linear chirp component (which is the 'nominal') , there are other linear chirps having different chirp rates. From figure 4.3.3c for Acquisition 1, it can been seen that there is even a faint up-chirp as well. However, these 'off-nominal' transmissions are significantly low in power compared to the nominal (~ 30 dB below).

4.3.3. Estimation of pulse-length and chirp-rate

Estimating the parameters of the received chirp signals is of paramount importance. A chirp signal is characterized by the chirp rate k_r and the duration of the chirp T_{pulse}. The bandwidth of the chirp B_r is related to these parameters by the following equation

$$B_r = |k_r| \cdot T_{pulse} \tag{4.3.2}$$

Figure 4.3.2 and 4.3.3 show the frequency spectrum and spectrograms of the acquired signals for Acquisition 1 and 2 respectively. The chirp rate in each case corresponds to the gradient of the the spectrogram. However, this is a coarse estimation and needs to be refined. A negative gradient implies a down-chirp.

For Acquisition 1 (referred with the subscript 1 in the following equations), the gradient in figure 4.3.3c is,

$$k_{r,est,1} = \frac{-50 - (50)}{14 - (-17.5)} = -3.1746 \times 10^{12} \text{ Hz/s}$$

The estimate is refined using the 'map drift' algorithm [18]. This method performs two 'looks' of pulse compression[2] using the estimated chirp rate, and finding the estimate error, $\triangle k_{r,a}$. Look 1 compresses the acquired chirp signal with one half of a reference linear FM chirp having chirp rate equal to the estimated, while look 2 compresses using the other half, as shown in the figure 4.3.6a.

The reference chirp is

$$s_{ref,est,1}(t) = \exp(j \cdot \pi \cdot k_{r,est,1} \cdot t^2) \tag{4.3.3}$$
$$S_{ref,est,1}(f) = F\{s_{ref,est,1}(t)\}$$

where F represents the Fourier Transform. Considering that the alias free Direct + Scattered signal in time is $s_{ds,1}(t)$ with Fourier Transform $S_{ds,1}(f)$, then the pulse compression outputs for look 1 and 2 are respectively,

$$X_{1,look\,1}(f) = S_{ds,1}(f) \cdot \{S_{ref,est,1}(f)\} \rfloor_{look\,1}\}^* \tag{4.3.4}$$

$$X_{1,look\,2}(f) = S_{ds,1}(f) \cdot \{S_{ref,est,1}(f)\} \rfloor_{look\,2}\}^* \tag{4.3.5}$$

$$x_{1,look\,1}(t) = F^{-1}\{X_{1,look\,1}(f)\}$$
$$x_{1,look\,2}(t) = F^{-1}\{X_{1,look\,2}(f)\}$$

where F^{-1} represents the inverse Fourier Transform. The offset between the two compression peaks $x_{1,look\,1}(t)$ and $x_{1,look\,2}(t)$ is called the 'mis-registration' error $\triangle x_1(t)$. The difference between the centers of the two looks is $\triangle f_a = 40 \times 10^6$ Hz. From the figure 4.3.6b, the mis-registration is,

$$\triangle x_1(t) = 2.321 \times 10^{-7} \text{ s}$$

Referring to [18], the error in the chirp-rate is given by,

$$\triangle k_{r,1} \approx -\frac{k^2_{r,est,1}}{\triangle f_a} \cdot \triangle x_1 \tag{4.3.6}$$

and the improved estimate is,

$$k_{r,1} = k_{r,est,1} - \triangle k_{r,1} \tag{4.3.7}$$

Hence, we get,

$$\triangle k_{r,1} \approx -5.8478 \times 10^{10} \text{ Hz/s} \tag{4.3.8}$$

$$k_{r,1} = -3.1746 \times 10^{12} - (-5.8478 \times 10^{10}) = -3.116 \times 10^{12} \text{ Hz/s} \tag{4.3.9}$$

Using equation1.1.5 and knowing that the transmit bandwidth was 150 MHz, we can then get the pulse length $T_{pulse,1}$ of the signal,

$$T_{pulse,1} = \frac{B_{r,1}}{|k_{r,1}|} \approx \frac{150 \times 10^6}{3.116 \times 10^{12}} = 47.378\ \mu\text{s} \tag{4.3.10}$$

[2]Pulse compression is discussed in detail in the chapter 5.

Figure 4.3.5.: Estimating the chirp-rate for Acquisition 1

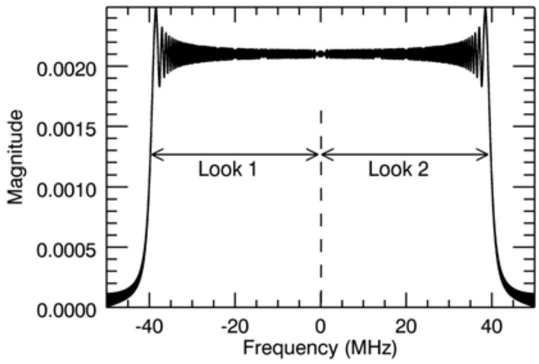

(a) Reference chirp, $S_{ref,est,1}(f)$

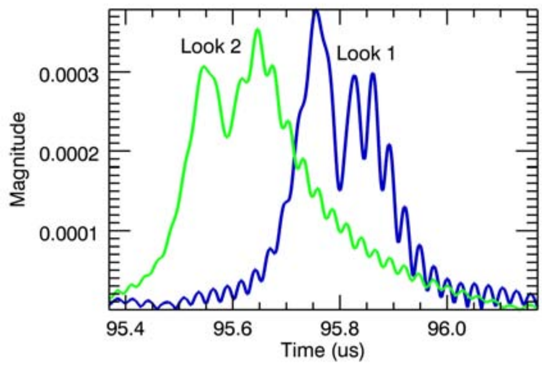

(b) Compressed looks, showing their mis-registration

Applying a similar procedure for Acquisition 2, first a coarse estimation of the chirp rate is obtained by measuring the gradient of the spectrogram in 4.3.4c.

$$k_{r,est,2} = \frac{40 - (-40)}{-25.3 - (26.5)} = -1.5444 \times 10^{12} \text{ Hz/s} \tag{4.3.11}$$

From figure 4.3.7a, the distance between the centers of the looks is,

$$\triangle f_a = 40 \times 10^6 \text{ Hz}$$

which is the same as before, and by measuring the mis-registration from figure 4.3.7b, we get,

$$\triangle x_2(t) = 1.392 \times 10^{-7} \text{ s}$$

The chirp rate error is,

$$\triangle k_{r,2} \approx -\frac{k_{r,est,2}^2}{\triangle f_a} \cdot \triangle x_2 = 8.30040 \times 10^9 \text{ Hz/s} \tag{4.3.12}$$

The improved estimate is,

$$k_{r,2} = 1.5361 \times 10^{12} \text{ Hz/s} \tag{4.3.13}$$

Similarly,

$$T_{pulse,2} = \frac{B_{r,2}}{|k_{r,2}|} \approx \frac{80 \times 10^6}{1.5361 \times 10^{12}} = 52.08\ \mu\text{s} \tag{4.3.14}$$

Figure 4.3.6.: Estimating the chirp-rate for Acquisition 2

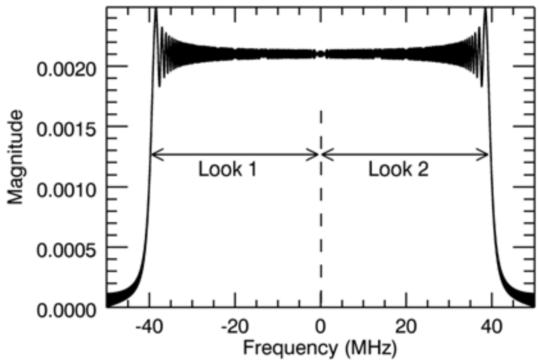

(a) Reference chirp, $S_{ref,est,2}(f)$

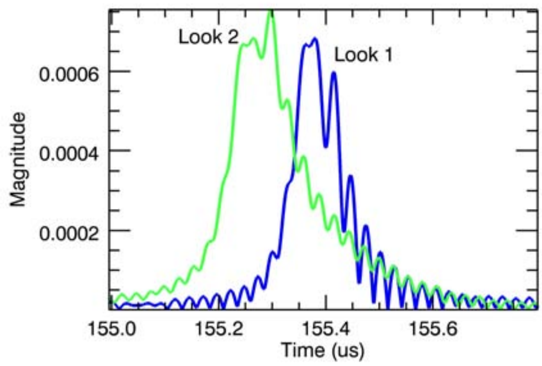

(b) Compressed looks, showing their mis-registration

4.4. Estimation of PRF and Pulse alignment

The acquired pulse trains are a 1-D stream of data. Converting it to a 2-D range and azimuth data is one of the main challenges with respect to the processing of the data. As SABRINA is a non-cooperative system, there is a lack of an explicit synchronization between the transmitter and the receiver, which implies that there is no explicit PRF signal at the receiver, and the transmitter and the receiver are not phase-locked to each other. This lack of phase synchronization leads to an unknown apparent Doppler shift [14]. In SABRINA data processing, the direct signal is used to recover the PRF signal, after which the acquired data is aligned and converted to 2-D range azimuth data matrix. The details of the methods to estimate the PRF and the Doppler shift, and the corresponding phase correction is referred to [14, 16, 17]. Figure 4.4.1 shows the 2-D data matrix after pulse alignment.

Figure 4.4.1.: 2-D data matrix in range and azimuth: Acquisition 2

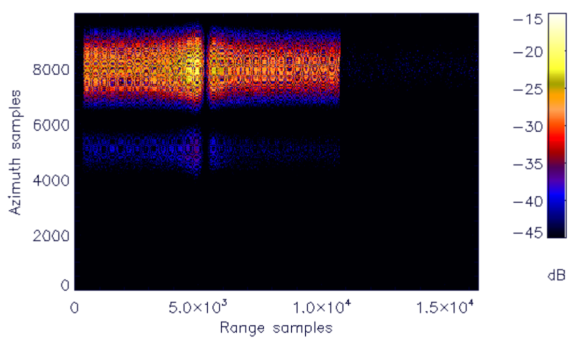

(a) Direct signal

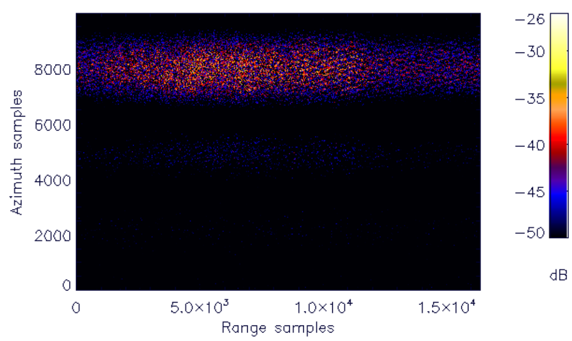

(b) Scattered signal

5. Range Compression

Range compression is an imperative step towards the processing of the acquired data. It refers to the pulse compression of the received chirp signal in range.

This chapter presents the problems in range compression of the acquired data, which result owing to the fact that the characteristics of the acquired chirps tend to vary from the nominal characteristics, such as the existence of a null at zero-frequency and unwanted resonances around it (as discussed in section 2.2.3). These are limitations introduced by the current SABRINA-X hardware. Moreover, the spectrograms presented in section 4.3.2 apprise us of the 'off-nominal' transmissions from the satellite itself.

As a first approach, the acquired signals for Acquisition 1 and Acquisition 2 are range compressed using reference chirps as computed in last chapter, section 4.3.3. The results obtained are analyzed. Afterwards, attempts are made to improve the compression.

5.1. Optimal compression

In the context of the radar signals, the transmitted chirp signal is backscattered by many targets, and therefore, the received signal is not a single chirp, rather it contains many time-delayed chirps with different amplitudes. In order to detect the targets with their corresponding time delay, the received signal $s_r(t)$ is match-filtered using a reference chirp which has the same characteristics as the one transmitted i.e. $s_t(t)$. This pulse compression based on match-filtering leads to the best possible signal-to-noise ratio (SNR) [19]. If the reference chirp is $s_{ref}(t) = s_t(t)$, then the optimal filter for compression is,

$$h_{opt} = s^*_{ref}(-t) \tag{5.1.1}$$

which is basically a complex conjugated, time-reversed replica of the reference chirp. The matched-filter output response is given by the following convolution,

$$x_{opt}(t) = s_r(t) \otimes h_{opt}(t) = s_r(t) \otimes s^*_{ref}(-t) \tag{5.1.2}$$

It can be implemented in the frequency domain as,

$$X_{opt}(f) = S_r(f) \cdot H_{opt}(f) = S_r(f) \cdot S^*_{ref}(f) \tag{5.1.3}$$

$$x_{opt}(t) = F^{-1}\{X_{opt}(f)\} \tag{5.1.4}$$

where F^{-1} represents inverse Fourier Transform. Figure 5.1.1 shows two targets ideally compressed.

Figure 5.1.1.: Ideally range compressed targets

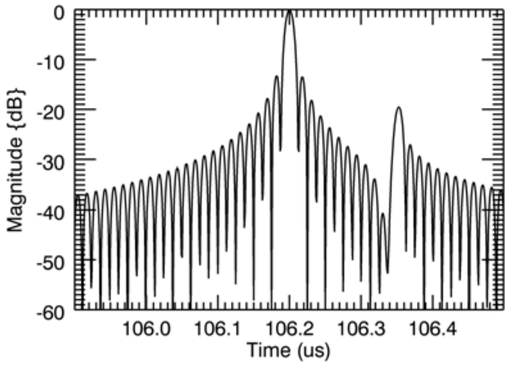

5.2. Range compression for Acquisition 1

A direct signal acquired dedicatedly would be the first choice to serve as the reference chirp signal for range compression. However, due to the considerations stated in section 3.2.2, the direct signal for acquisition 1 was not acquired dedicatedly; instead, it was acquired combined with the scattered (i.e. the 'Direct + Scattered' signal). Therefore, the initial approach towards the range compression is to use a linear chirp with the parameters as estimated in section 4.3.3, as the reference signal for pulse compression.

5.2.1. Compression using a linear FM chirp with estimated parameters

Defining a linear FM chirp with parameters as estimated in 4.3.3, i.e. with a chirp rate $k_{r,1}$ as given in equation 4.3.9, and pulse length $T_{pulse,1}$as given in equation 4.3.10, we get,

$$s_{ref,1}(t) = \exp(j \cdot \pi \cdot k_{r,1} \cdot t^2) \tag{5.2.1}$$
$$-\frac{T_{pulse,1}}{2} \leq t \leq \frac{T_{pulse,1}}{2}$$

The range compression filter is then,

$$h_1(t) = s^*_{ref,1}(-t)$$

The Direct + Scattered signal (after anti-alias filtration) $s_{ds,1}(t)$ is range compressed using this filter.

$$X_{ds,1}(f) = S_{ds,1}(f) \cdot H_1(f) = S_{ds,1}(f) \cdot S^*_{ref,1}(f) \tag{5.2.2}$$
$$x_{ds,1}(t) = F^{-1}\{X_{ds,1}(f)\}$$

Figure 5.2.1.: Range compression of the Direct + Scattered signal using a linear chirp with precisely estimated chirp rate and pulse length

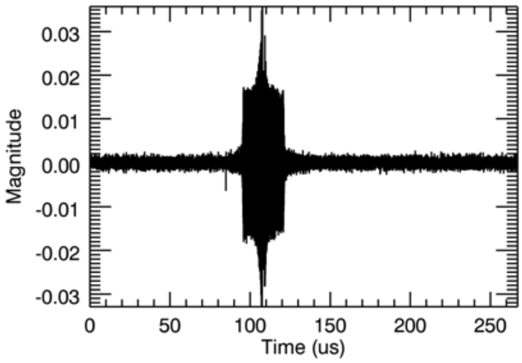

(a) Received chirp, $Re\{s_{ds,1}(t)\}$

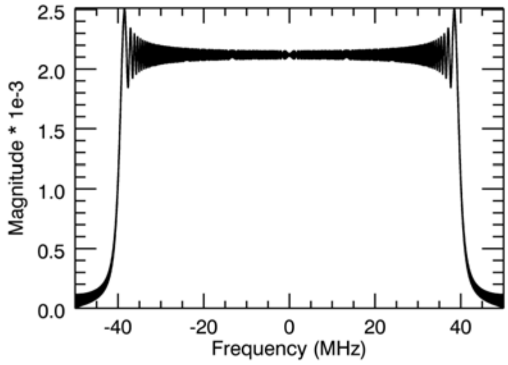

(c) $|S_{ref,1}(f)|$

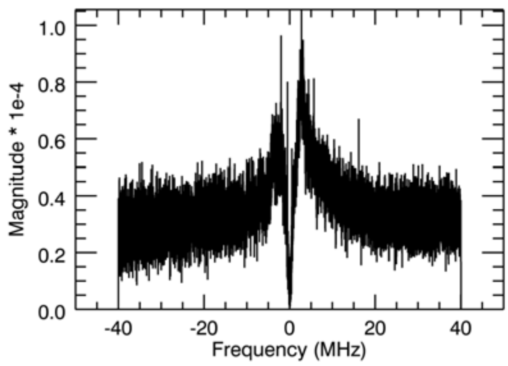

(b) $|S_{ds,1}(f)|$

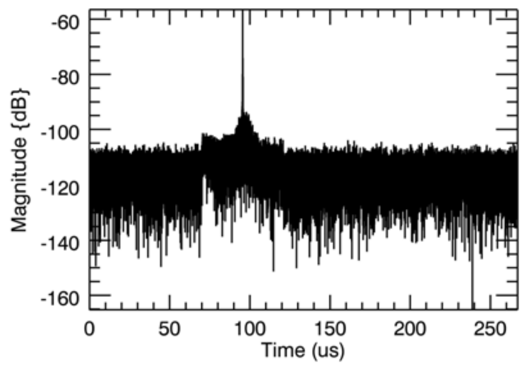

(d) $|x_{ds,1}(t)|$

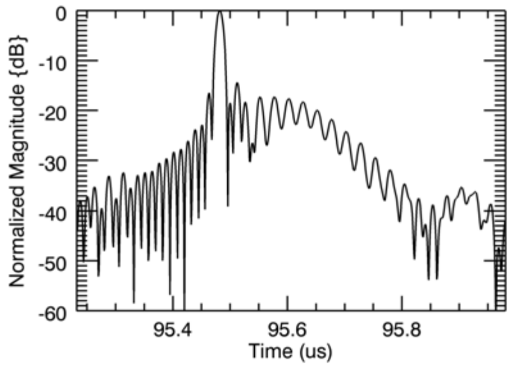

(e) $|x_{ds,1}(t)|$ Zoomed: Peak of the Direct signal, followed by unwanted 'tail' effect

Figure 5.2.2 shows the range compression. The peak existing in the compressed output in figure 5.2.2d corresponds to the direct signal, which is much more powerful compared to the scattered contribution in the combined acquired signal.

From the zoomed look in figure 5.2.2e, it can be seen that the compression output peak is followed by a 'tail'. The existence of this tail implies a degraded compression. It needs to appreciated here, however, that a perfect compression (as for the optimal case in the last section) was not expected, keeping in view the fact that the hardware had introduced the undesired resonance around the null at zero-frequency in the spectrum of the acquired signals, and the transmission from the satellite was off-nominal too.

5.2.2. Compression using an improved matched filter

This section builds on the compression results of the last section, and strives to improve them by suppressing the 'tail' effect. The compressed output from the last section is, in a sense, reprocessed to dampen the tail. It is first widowed from the peak to the tail end, and then this windowed signal $x_{ds,1,w}(t)$ (shown in figure 5.2.3a) is passed to a 'phase-equalizer and resonance damping' filter $h_a(t)$. In frequency domain, we have

$$X_{ds,1,w}(f) = F\{x_{ds,1,w}(t)\}$$

$$H_a(f) = F\{h_a(t)\}$$

and $H_a(f)$ is given by,

$$H_a(f) = \frac{|X_{ds,1,w}(f)|}{X_{ds,1,w}(f)} \cdot A(f) \tag{5.2.3}$$

where $A(f)$ is an array of real values in the frequency domain to flatten the resonance peaks in the frequency spectrum (by simple amplitude modulation of the spectrum, as shown in figure 5.2.3).

The output after filtering the windowed signal with $H_a(f)$ is,

$$Y_{ds,1,w}(f) = H_a(f) \cdot X_{ds,1,w}(f) \tag{5.2.4}$$

$$y_{ds,1,w}(t) = Y_{ds,1,w}(f)$$

Comparing figure 5.2.3a and figure 5.2.3d, we can notice that the tail has been suppressed.

The new filter for range compression is then,

$$H_{imp} = H_1(f) \cdot H_a(f) \tag{5.2.5}$$

The output after applying the above filter on the received signal is,

$$X_{ds,imp,1}(f) = H_{imp}(f) \cdot S_{ds,1}(f) \tag{5.2.6}$$

Figure 5.2.2.: Range compression of the Direct + Scattered signal using the improved match filtration

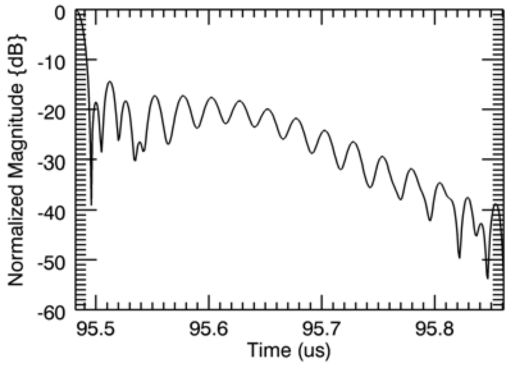

(a) $x_{ds,1,w}(t)$

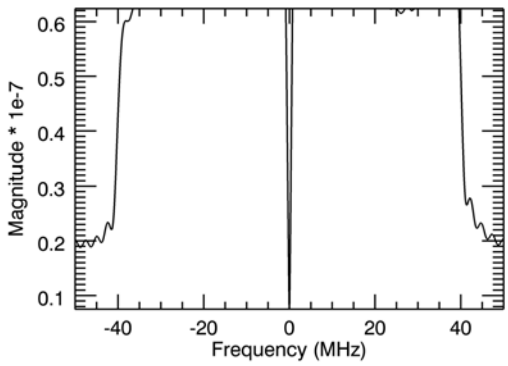

(c) $Y_{ds,1,w}(f)$

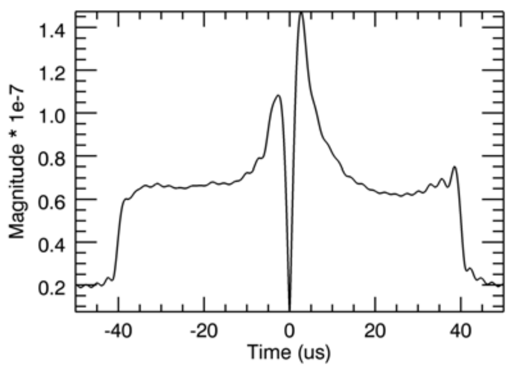

(b) $X_{ds,1,w}(f)$

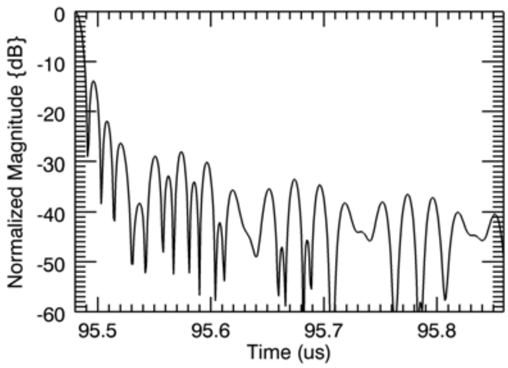

(d) $y_{ds,1,w}(t)$

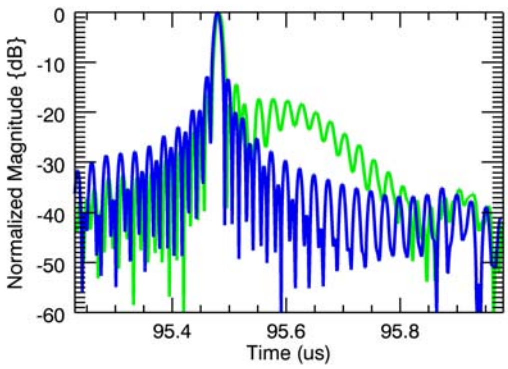

(e) Range compression with $H_{imp}(f)$ i.e. $x_{ds,imp,1}(t)$ [blue], and with $H_1(f)$ i.e. $x_{ds,1}(t)$ [Green]

Figure 5.2.3.: $A(f)$ (for flattening the resonances in the spectra of the acquired signals)

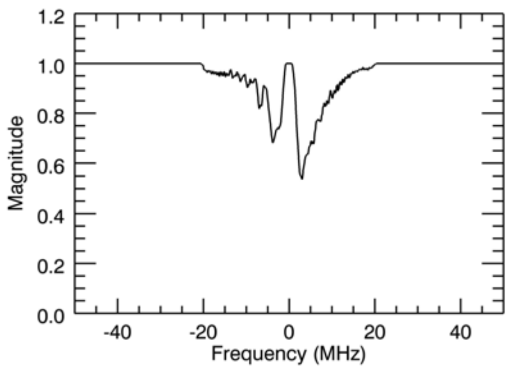

$$x_{ds,imp,1}(t) = F^{-1}\{X_{ds,imp,1}(f)\}$$

Figure 5.2.3e clearly shows that the new filter has improved compression. It must, however, be noted that this comparison is in terms of the absolute values of the compressed outputs, and not explicitly in terms of phase. Using equation 5.2.3 and equation 5.2.5, the improved filter has a phase response of,

$$\angle\{H_{imp}(f)\} = \angle\{H_1(f)\} - \angle\{X_{ds,1,w}(f)\} \tag{5.2.7}$$

The SAR interferograms are sensitive to the phase response of the compressed outputs. We can get a qualitative comparison between the filters by observing the interferograms respectively generated.

5.2.3. Compression using a previously recorded direct signal

On October 20, 2009, an acquisition campaign was performed acquiring TerraSAR-X signals transmitted in stripmap mode. The hardware of SABRINA-X was not optimized as yet for the acquisition of TerraSAR-X signals. It lacked the additional 48.5 MHz cut-off filters in the baseband circuitry; and therefore, prior to sampling at 100 MS/s, the signals were highly aliased as shown in the spectrogram in figure 5.2.4. After anti-alias filtration, only 40 MHz of bandwidth is retained.

In this campaign (referred as the ‘Acquisition 0’ onwards), the direct signal from the satellite was dedicatedly acquired. It was observed that this signal had the same parameters as the one for Acquisition 1. Therefore, for the sake of investigation, the Direct + Scattered signal of Acquisition 1 (i.e. $s_{ds,1}(t)$) was matched filtered using this direct signal as the reference signal.

Prior to match-filtering, the signal $s_{ds,1}(t)$ was filtered to 40 MHz bandwidth because the direct signal of Acquisition 0, $s_{d,0}(t)$ contains only 40 MHz of alias-free bandwidth. The compressed

Figure 5.2.4.: Spectrogram of direct signal acquired in October 2009

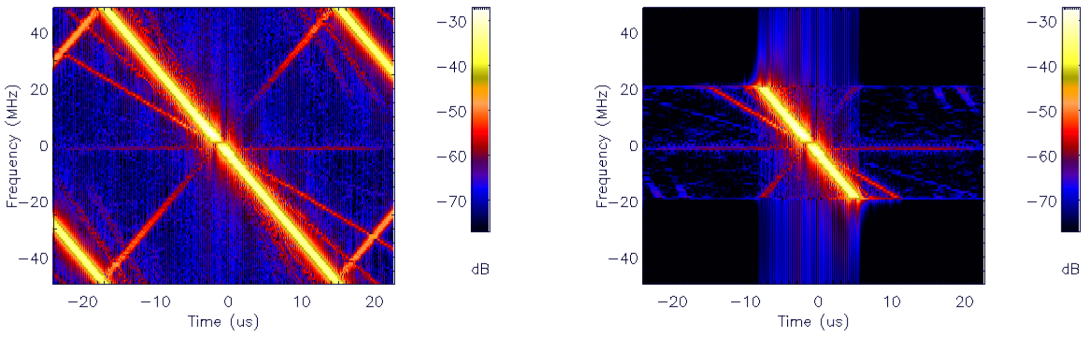

(a) Before anti-alias filtration

(b) After anti-alias filtration

output is,

$$\grave{x}_{ds,1}(t) = F^{-1}\{S_{ds,1}(f) \cdot S^{*}_{d,0}(f)\}$$

We can try to improve the compression by flattening the frequency spectra of the acquired signals (i.e. suppressing the resonances) with $A(f)$,

$$\breve{x}_{ds,1}(t) = F^{-1}\{[S_{ds,1}(f) \cdot A(f)].[S^{*}_{d,0}(f) \cdot A(f)]\} \tag{5.2.8}$$

$$\breve{x}_{ds,1}(t) = F^{-1}\{[S_{ds,1}(f).S^{*}_{d,0}(f) \cdot A^{2}(f)]\} \tag{5.2.9}$$

Results are presented in figure 5.2.5. A slight improvement can be seen with flattening of the spectra suppressing resonance peaks.

5.2.4. Conclusion

The figure 5.2.3e clearly depicts that the improved filter $H_{imp}(f)$ provides a significantly better compression, eliminating the tail effect. Direct signal from Acquisition 0 can also be used to range compress acquired signals of Acquisition 1; however, since the bandwidth of this direct signal is only 40 MHz as against an 80 MHz bandwidth of the Direct + Scattered signal, there would be a reduction in range resolution (as per the equation 1.2.2).

Figure 5.2.5.: Range compression of the Direct + Scattered signal using the direct signal of Acquisition 0

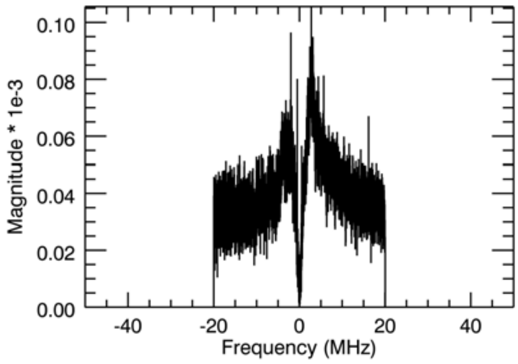

(a) $S_{ds,1}(f)$ (filtered to 40 MHz bandwidth)

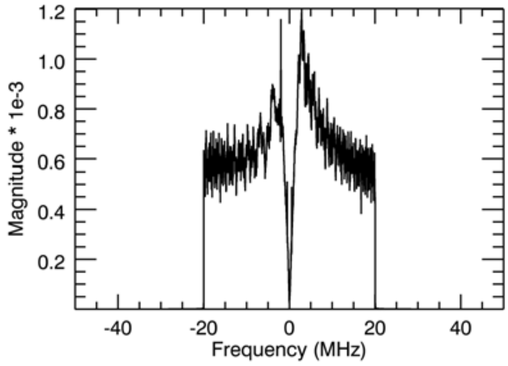

(c) $S_{d,0}(f)$ after anti-alias filtration

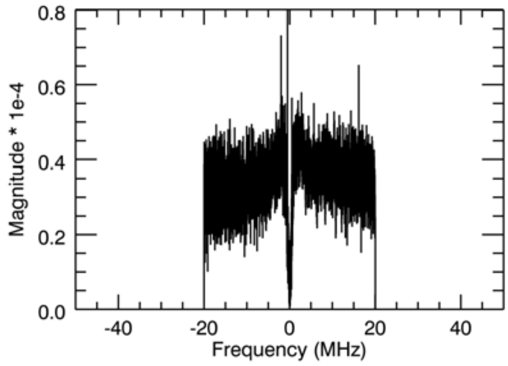

(b) $S_{ds,1}(f)$ (resonance suppressed)

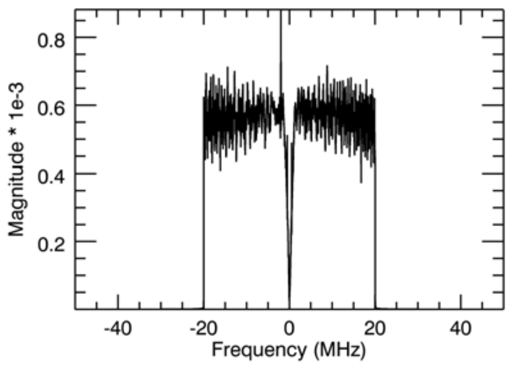

(d) $S_{d,0}(f)$ (resonance suppressed)

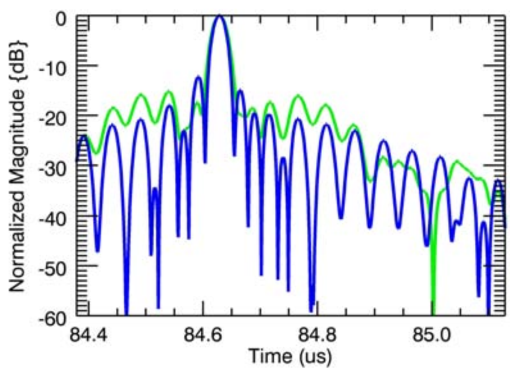

(e) Range compression $\grave{x}_{ds,1}(t)$ [Green] and $\breve{x}_{ds,1}(t)$ [blue]

5.3. Range compression for Acquisition 2

For acquisition 2, the direct signal from the satellite was acquired directly. To arrive at the most appropriate filter for the compression, we proceed by compressing the direct signal with itself (with and without suppressing the resonance peaks), and with a linear FM chirp with parameters as estimated in 4.3.3 for comparison. Figure 5.3.1 summarizes all these three options.

5.3.1. Compression using a linear FM chirp with estimated parameters

Defining a linear FM chirp with parameters as estimated in 4.3.3, i.e. with a chirp rate $k_{r,2}$ as given in equation 4.3.13, and pulse length $T_{pulse,2}$ as given in equation 4.3.14, we get,

$$s_{ref,2}(t) = \exp(j \cdot \pi \cdot k_{r,2} \cdot t^2) \tag{5.3.1}$$

$$-\frac{T_{pulse,2}}{2} \leq t \leq \frac{T_{pulse,2}}{2}$$

The range compression filter is then,

$$h_2(t) = s^*_{ref,2}(-t)$$

If the acquired direct signal is $s_{d,2}(t)$, then the corresponding compression output is,

$$x_{d,2}(t) = F^{-1}\{S_{d,2}(f) \cdot H_2(f)\} = F^{-1}\{S_{d,2}(f) \cdot S^*_{ref,2}(f)\} \tag{5.3.2}$$

The results are shown in figure 5.3.1.

5.3.2. Compression with the acquired direct signal

Matched-filtering the acquired direct signal $s_{d,2}(t)$ with itself, we get

$$\grave{x}_{d,2}(t) = F^{-1}\{S_{d,2}(f) \cdot S^*_{d,2}(f)\} \tag{5.3.3}$$

In case of suppressing the resonance in the frequency spectrum, we get

$$\breve{x}_{d,2}(t) = F^{-1}\{[S_{d,2}(f).S^*_{d,2}(f) \cdot A^2(f)]\} \tag{5.3.4}$$

The results are shown in figure 5.3.1.

Figure 5.3.1.: Range compression of the direct signal of Acquisition 2

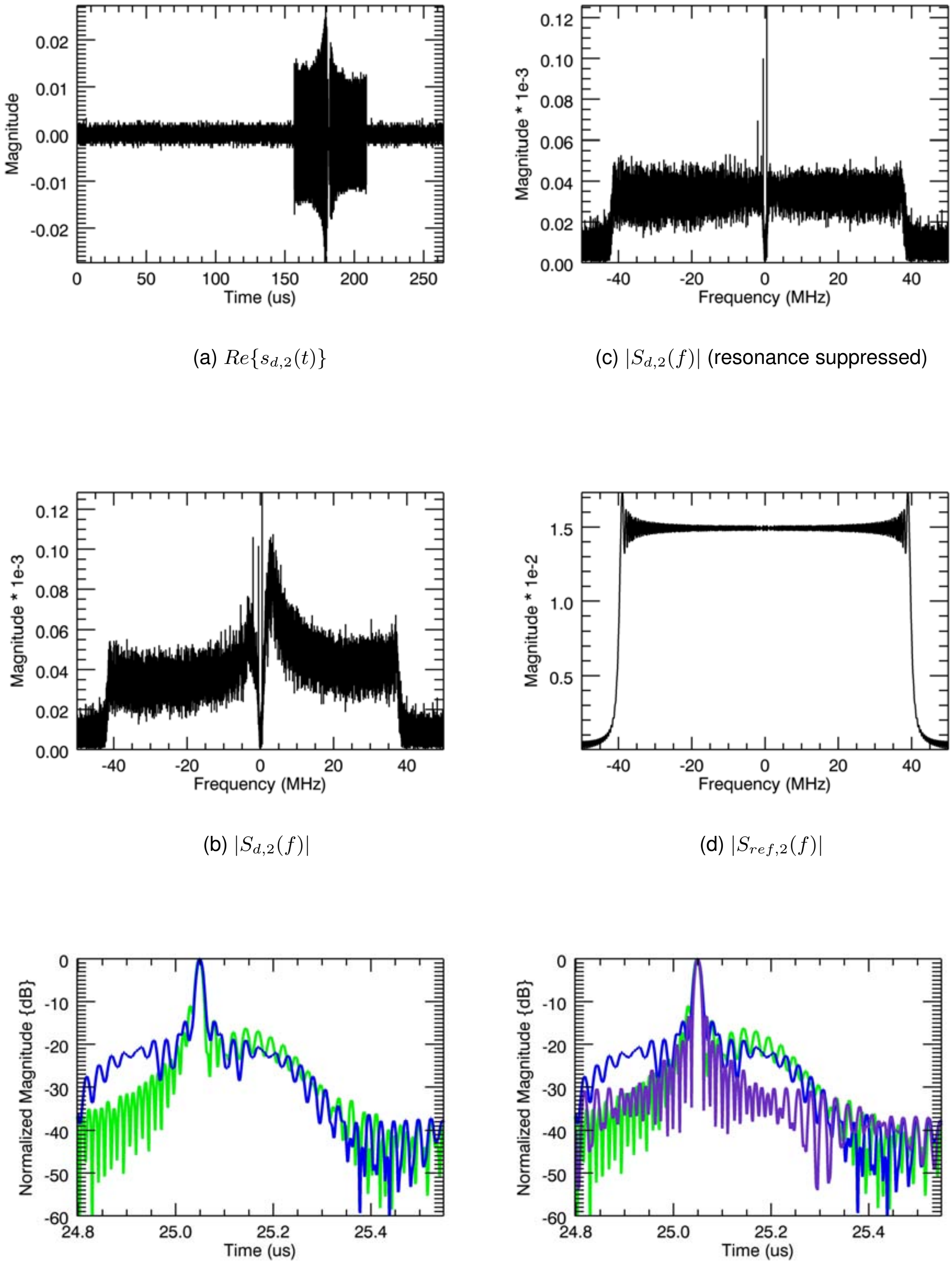

(a) $Re\{s_{d,2}(t)\}$

(c) $|S_{d,2}(f)|$ (resonance suppressed)

(b) $|S_{d,2}(f)|$

(d) $|S_{ref,2}(f)|$

(e) $x_{d,2}(t)$ [Green] and $\grave{x}_{d,2}(t)$ [Blue]

(f) $x_{d,2}(t)$ [Green], $\grave{x}_{d,2}(t)$ [Blue] and $\breve{x}_{d,2}(t)$ [Purple]

5.3.3. Conclusion

From figure 5.3.2e, it is apparent that the pulse compression using the direct signal as reference is better. Moreover, as depicted by figure 5.3.2f, the suppression of resonance peaks further improves the compression.

6. Results

This chapter presents the results in terms of Bistatic SAR reflectivity images and interferograms generated after the processing of the raw data, in range and azimuth. Range processing is performed with the different compression filters explored in the last chapter. The details of the SABRINA processing steps are referred to [14, 16, 17].

6.1. Bistatic SAR images

6.1.1. Acquisition 1

The signals acquired as per the Acquisition 1 are: 'Direct + Scattered' and 'Scattered (only)'. Since the Direct + Scattered signal contains the backscattered data besides the direct signal from the satellite, it is also processed like the Scattered to yield two reflectivity images of the viewed terrain.

Figure 6.1.1 shows the viewed terrain at the time of the satellite pass (i.e. at the time of the acquisition of the signals). It is expected that the reflectivity images correspond to the viewed terrain at the time.

The figures on the following pages show the images obtained with the different compression techniques as explored in the last chapter, for both the Direct + Scattered signal and the Scattered signal. These images correspond to the backscatter of the terrain towards the receiver. The images depict the features of the terrain. The images of the Direct + Scattered signal have a horizontal azimuth line seemingly extending over the entire range with a high power. This corresponds to the direct signal compressed in range (with it's strong side-lobes extending over the entire range). The point where this line cuts the zero-range axis corresponds to the position of the antenna acquiring the signal.

Figure 6.1.8 shows a zoomed look at the images to compare the compression outputs in range. The 'tails' generated by range compression using a linear FM chirp (with estimated parameters) are clearly visible. Due to the existence of these tails, this method of range compression is rendered unsuitable for processing the SAR images (and subsequent interferometry). These tails are suppressed by using $H_{imp}(f)$ filter for range compression.

The range compression performed using the direct signal of Acquisition 0 (as shown in 6.1.8) involves suppressing the resonances, as discussed in section 5.2.3. The compressed output does not have any 'tails'.

Figure 6.1.1.: Viewed Terrain: Acquisition 1

(a) Viewed terrain (optical image) at the time of the satellite passage and signal acquisition

(b) Google view of the viewed terrain

Figure 6.1.2.: Image for the Direct + Scattered signal, using a linear FM chirp with estimated parameters for range compression

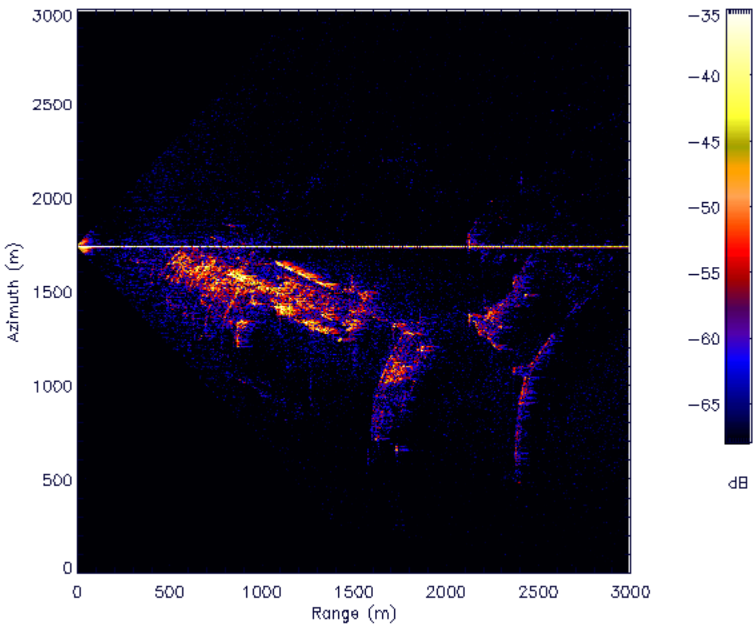

Figure 6.1.3.: Image for the Direct + Scattered signal, using the $H_{imp}(f)$ for range compression

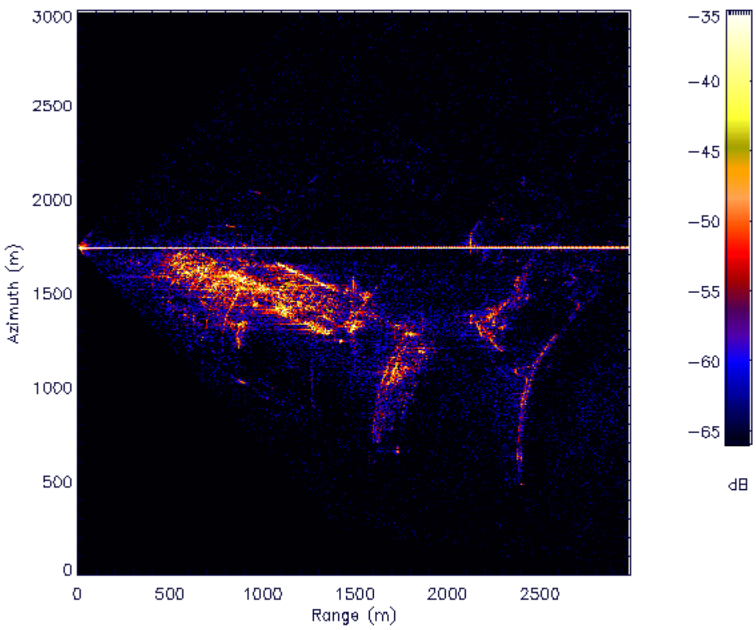

Figure 6.1.4.: Image for the Direct + Scattered signal, using the direct signal from Acquisition 0 for range compression

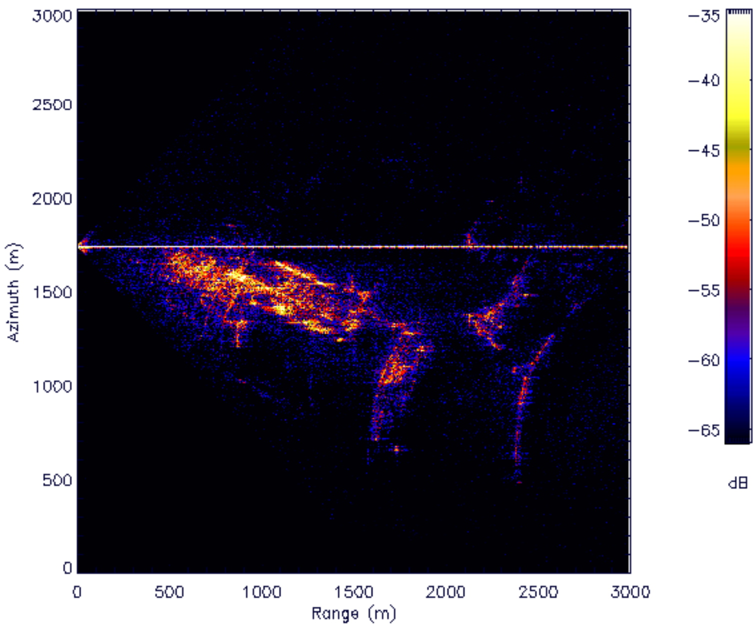

Figure 6.1.5.: Image for the scattered signal, using a linear FM chirp with estimated parameters for range compression

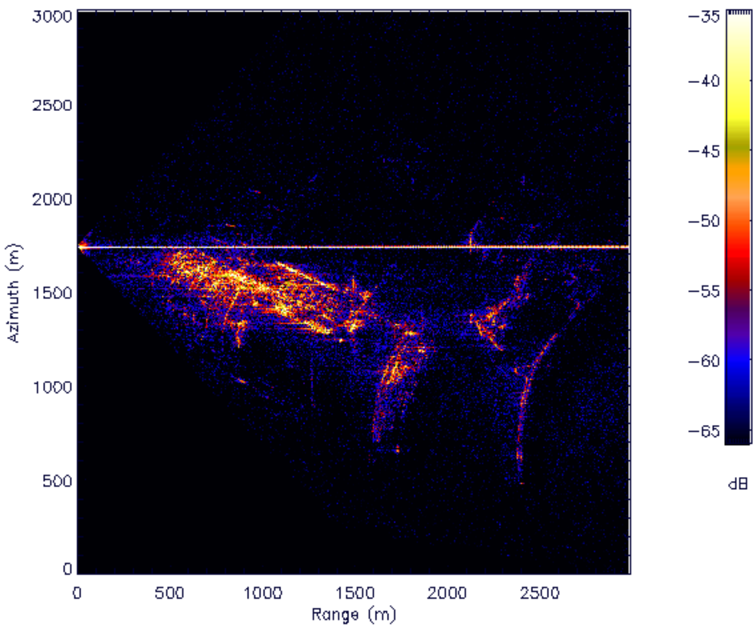

Figure 6.1.6.: Image for the scattered signal, using $H_{imp}(f)$ for range compression

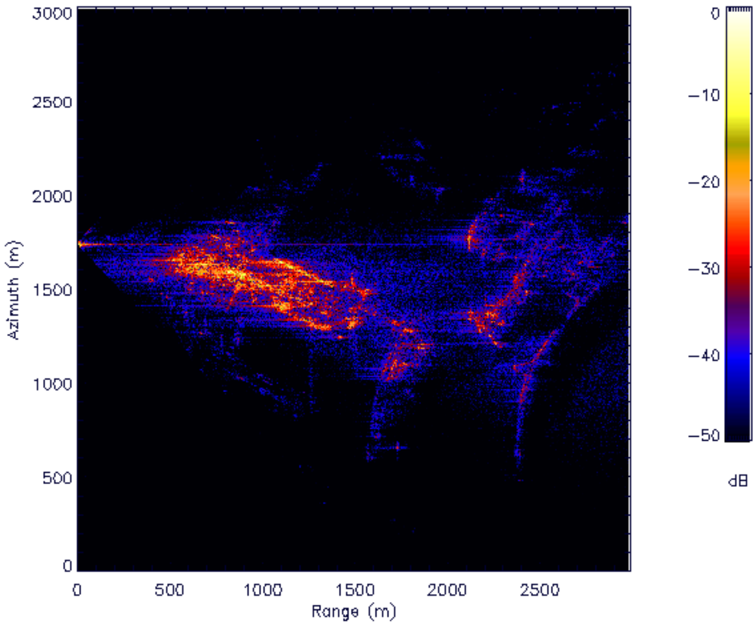

Figure 6.1.7.: Image for the scattered signal, using the direct signal from Acquisition 0 for range compression

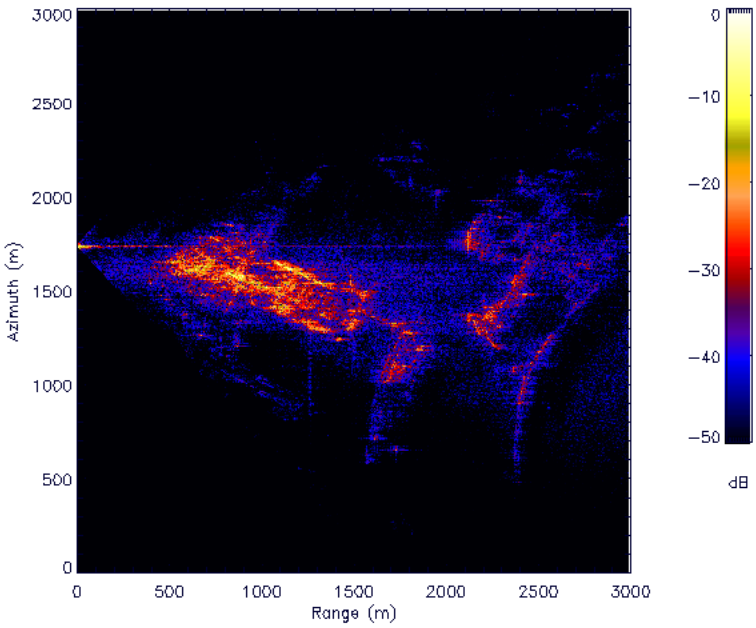

Figure 6.1.8.: Zoomed look at the scattered signal images to compare the range compression filters

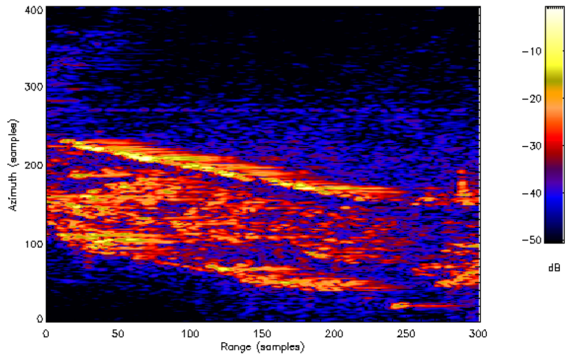

(a) Using a linear FM chirp with estimated parameters: 'tail' effect visible

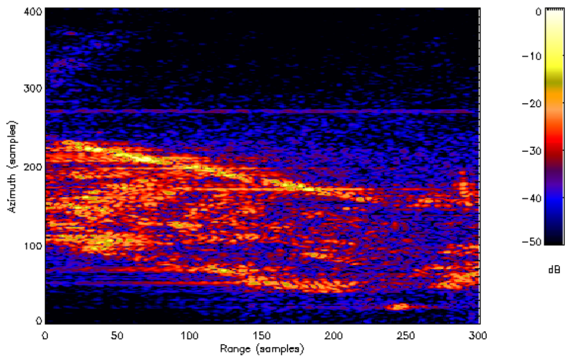

(b) Using the $H_{imp}(f)$ for range compression: 'tail' effect suppressed

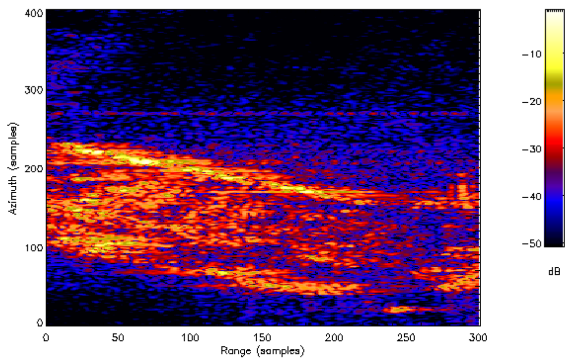

(c) Using the direct signal from Acquisition 0 for range compression

Figure 6.1.9.: Image of the scattered signal from Acquisition 2, with range compression using the acquired direct signal

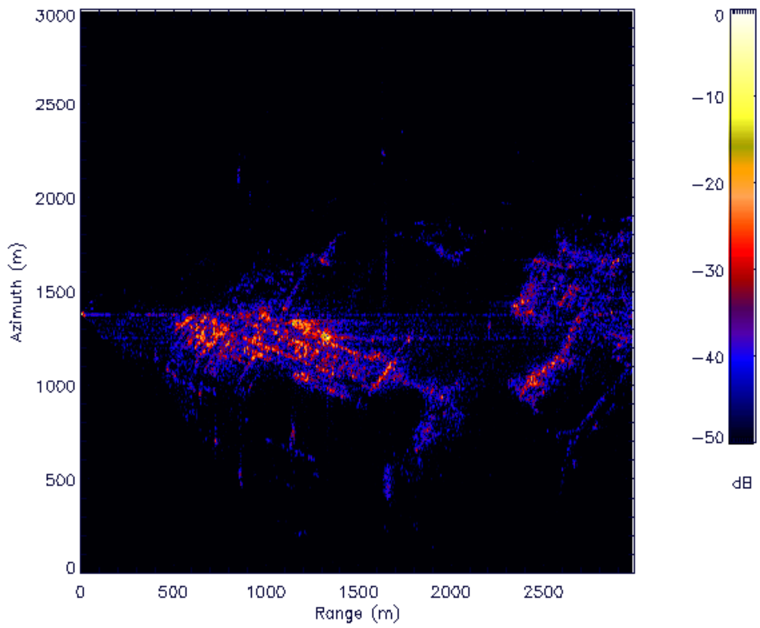

6.1.2. Acquisition 2

For the case of acquisition 2, figure 6.1.9 shows the image obtained. The range compression is performed using the acquired direct signal (with resonance suppression). The corresponding optical image of the viewed terrain is given in figure 3.1.1.

6.2. Interferograms

Interferograms in the bistatic SAR context are phase images obtained by phase subtraction of two SAR images obtained with slightly separated receiving antennas. If the the antennas are stacked vertically, as for the Acquisition 1, the interferogram can be processed in order to obtain detailed topography once the systematic phase differences (fringes) due to the slant observation of the Earth surface have been removed. It is referred to as 'across-track' interferometry.

Interferograms are processed for the case of Acquisition 1 as we have two images of the viewed terrain in this case (one corresponding to the Direct + Scattered signal and the other to the Scattered signal). Figure 6.3.2 shows two interferograms; one is obtained with images that have been range processed with $H_{imp}(f)$, while the other is obtained with images having been range processed with the direct signal from Acquisition 0.

Figure 6.2.1.: Interferograms

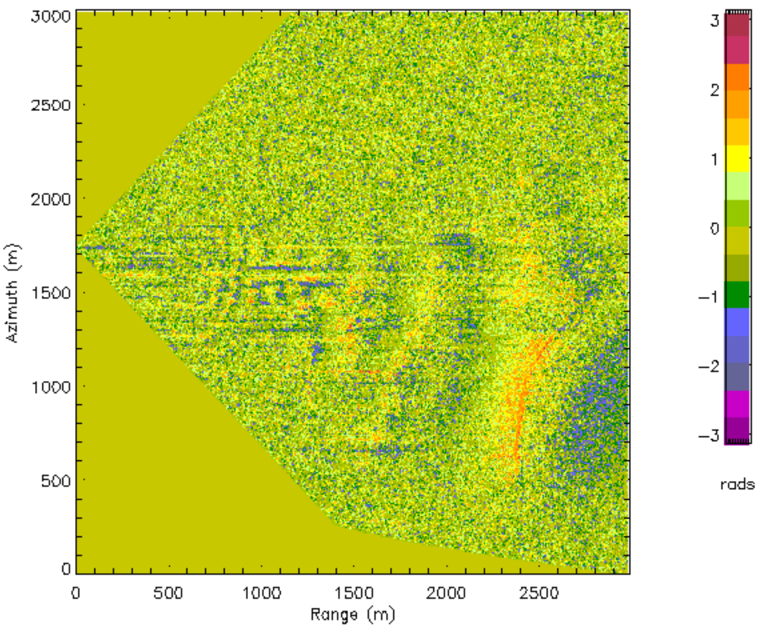

(a) Processed with the images range compressed using $H_{imp}(f)$

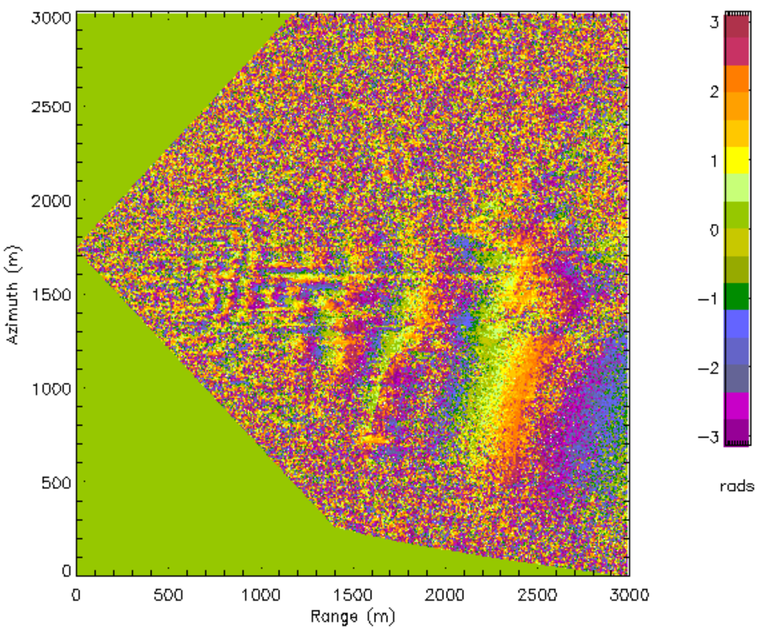

(b) Processed with the images range compressed using the direct signal from Acquisition 0

Figure 6.3.1.: Geocoded Image

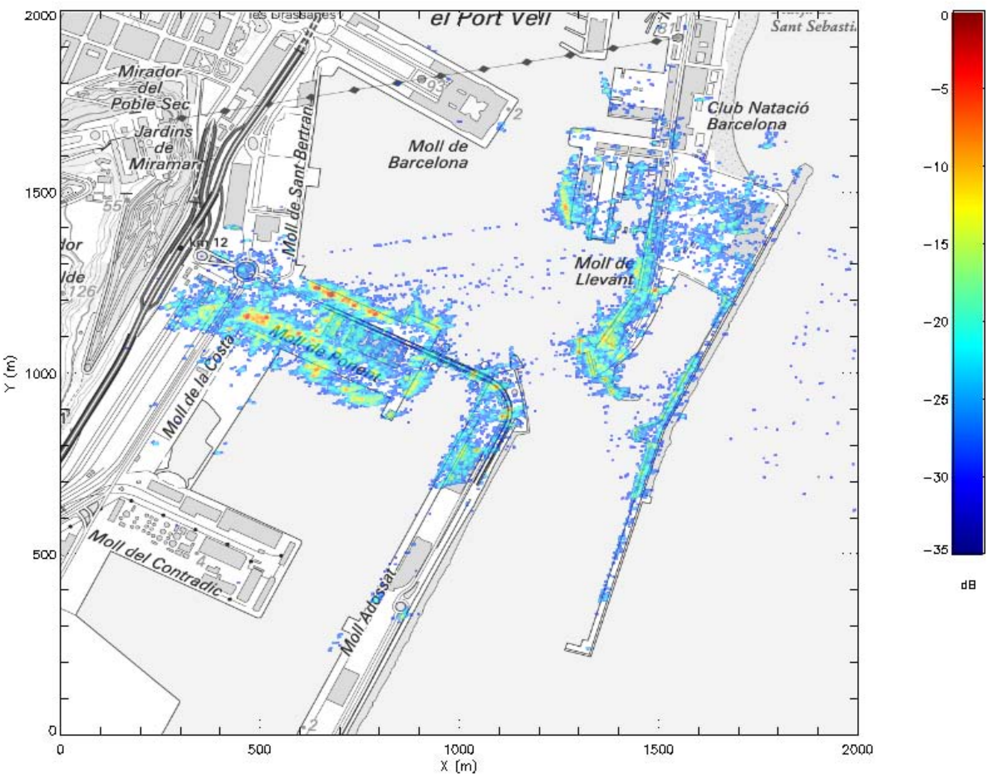

The interferogram in figure 6.2.2a has a poor quality; we don't see any 'fringes' that are expected due to the flat-earth component of the viewed terrain. These fringes are visible in the other interferogram, in figure 6.2.2b.

This observation implies that although the filter $H_{imp}(f)$ serves well for range compression (by suppressing 'tails') to get reflectivity images, it, however, is inappropriate for use to process interferograms. Moreover, it can be asserted now that the range compression using the direct signal (dedicatedly acquired) has good performance as regards getting reflectivity images as well as interferometry.

6.3. Geocoded results

This section presents the geo-coded reflectivity image and interferogram, obtained for the case of range compression using direct signal from Acquisition 0. Figure 6.3.1 shows the geocoded image. The images corresponds very well to the terrain features. Figure 6.3.2 shows the geocoded interferograms: figure 6.3.3a shows the interferogram with 'fringes' contributed by the flat-earth. It can be compensated for by removing the phase contribution due to the elevation characteristics of the terrain i.e. DEM compensation, as shown in figure 6.3.3b.

Figure 6.3.2.: Geocoded Interferograms

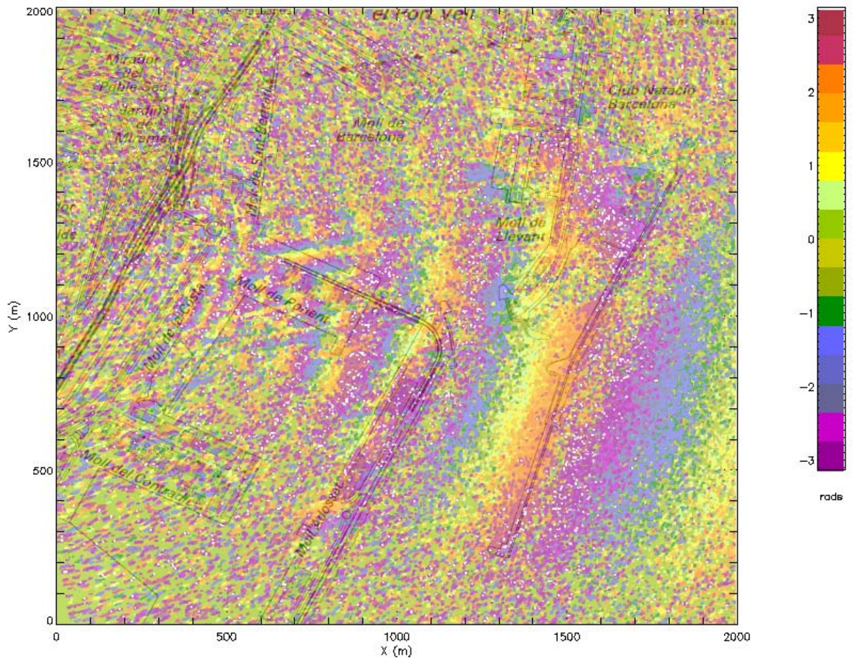

(a) Before DEM compensation

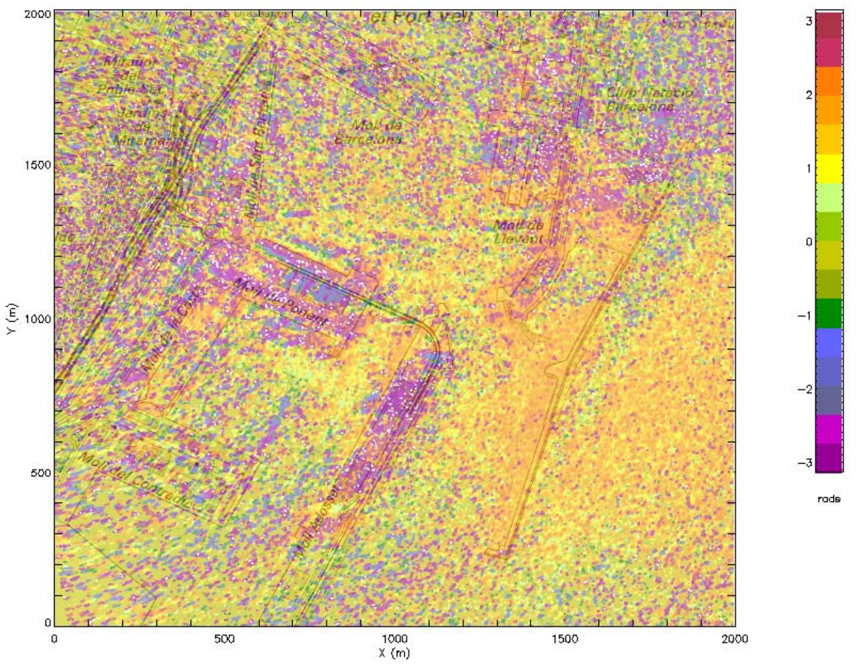

(b) After DEM compensation

Figure 6.3.3.: Zoomed DEM compensated interferogram highlighting the phase changes caused by terrain features

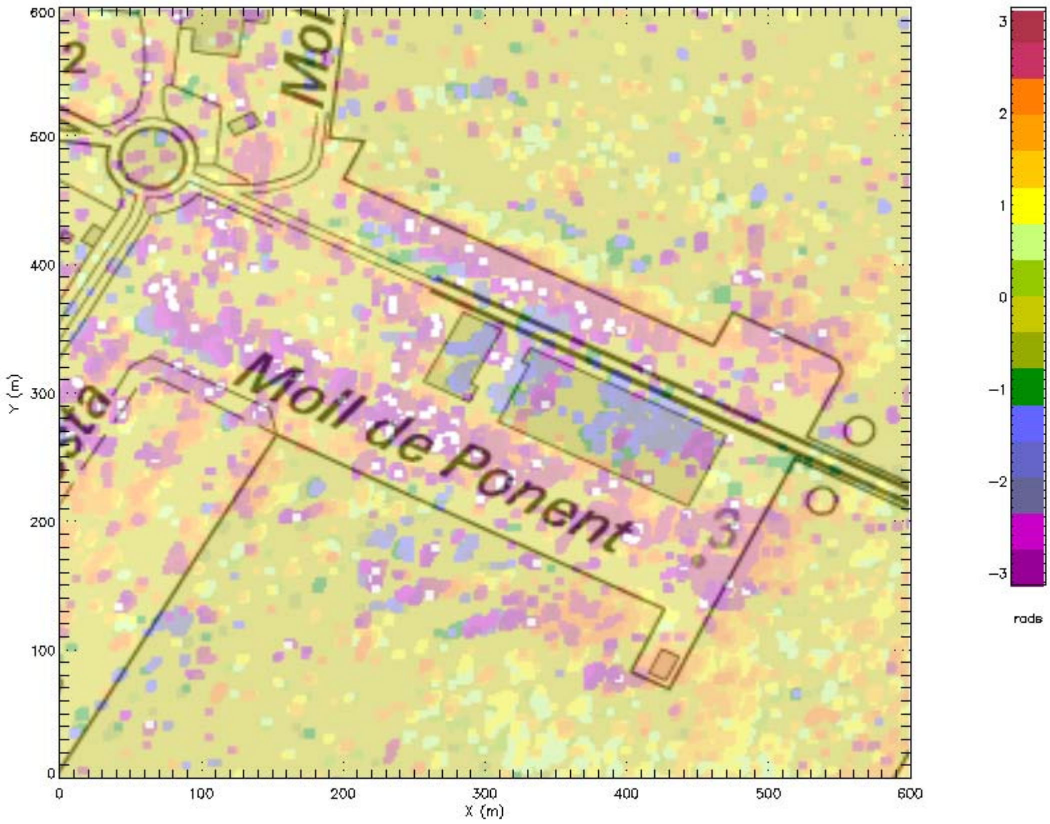

6.4. Conclusion

The results presented in this chapter and the analysis performed in the previous chapters lead to the following important inferences:

- It is of paramount importance to acquire the direct signal from the satellite 'dedicatedly', i.e. not as a combined acquisition with the scattered signal. This direct signal is not only important with respect to the recovery of PRF and phase synchronization (prior to subsequent formulation of the 2-D raw range-azimuth matrix), but also to serve as the reference signal for range compression such that both the reflectivity images and interferograms are obtained with good quality.

- In case of an absence of a dedicated (clean) direct signal, the filter $H_{imp}(f)$, as devised in section 5.2.2, can be used to range compress the acquired signals. It is an appropriate filter for obtaining the images, but not interferograms.

- Keeping in view that the hardware introduces resonances in the spectra of the acquired signals, and that the satellite transmissions can be 'off-nominal' (i.e. contaminated with multiple linear FM chirps with different chirp rates), range compression with a linear FM chirp as a matched filter does not provide efficient compression. It has been seen that in such a case, 'tails' tend to trail the compression peaks.

Bibliography

[1] McCandles, S.W., Jr.; "The origin, evolution and legacy of SEASAT," Geoscience and Remote Sensing Symposium, 2003. IGARSS '03. Proceedings. 2003 IEEE International , vol.1, no., pp. 32- 34 vol.1, 21-25 July 2003

[2] Duque, S.; Lopez-Dekker, P.; Mallorqui, J. J.; "Single-Pass Bistatic SAR Interferometry Using Fixed-Receiver Configurations: Theory and Experimental Validation," Geoscience and Remote Sensing, IEEE Transactions on , vol.48, no.6, pp.2740-2749, June 2010

[3] Mario.F. Hernández; "Design and implementation of a Bistatic Radar Receiver for TerraSAR-X", December 2009, PFC (Director: Prof. Dr. Antoni Broquetas), RSLab, UPC

[4] Wiesbeck, W.; "Lecture Script: Radar Systems Engineering", 15th edition, Institut für Hochfrequenztechnik und Elektronik (IHE), WS 2008/09

[5] Skolnik, I. Merrill; "Introduction to Radar Sytems", 3rd edition, McGraw-Hill Book Company, International Edition 1981

[6] Sherwin, C. W., J. P. Ruina, and R. D. Rawcliffe; "Some Early Developments in Synthetic Aperture Radar Systems", IRE Trans. Military Electronics, Vol. MIL-6, No.2, April 1962, pp. 111-115

[7] Moreira, Alberto; "Lectures: Spacborne SAR Remote Sensing", Microwave and Radar Institute, DLR, May 2009

[8] Sanz-Marcos, J.; Lopez-Dekker, P.; Mallorqui, J.J.; Aguasca, A.; Prats, P.; "SABRINA: A SAR Bistatic Receiver for Interferometric Applications," Geoscience and Remote Sensing Letters, IEEE , vol.4, no.2, pp.307-311, April 2007

[9] German Aerospace Center: TerraSAR-X [Online]. Available: `http://www.dlr.de/en/desktopdefault.aspx/tabid-4219/8885_read-15979/`

[10] Inforterra; TerraSAR-X: Mission and Satellite [Online]. Available: `http://www.infoterra.de/terrasar-x/terrasar-x-satellite-mission.html`

[11] Infoterra GMBH Initiates Commercial Exploitation of Terrasar-X[Online]. Available: `http://www.gisdevelopment.net/technology/sar/me05_062pf.htm`

[12] Layout Guidelines for MMIC Components [Online]. Available: `http://hittite.com/content/documents/layout_guidelines_for_mmic_components.pdf`

[13] F. R. Hoots and R. L. Roehrich, "Models for propagation of NORAD element sets," Aerosp. Defense Center, Peterson AFB, Colorado Springs, CO, Spacetrack Rep. 3, Dec. 1980.

[14] Sanz-Marcos, J.; Lopez-Dekker, P.; Mallorqui, J.J.; Aguasca, A.; Prats, P.; , "SABRINA: A SAR Bistatic Receiver for Interferometric Applications," Geoscience and Remote Sensing Letters, IEEE , vol.4, no.2, pp.307-311, April 2007

[15] Celestrack (via Center for Space Standards and Innovation (CSSI)): [Online]. Available:http://celestrak.com/columns/v04n03/#FAQ01

[16] Lopez-Dekker, P.; Mallorqui, J.J.; Serra-Morales, P.; Sanz-Marcos, J.; , "Phase Synchronization and Doppler Centroid Estimation in Fixed Receiver Bistatic SAR Systems," Geoscience and Remote Sensing, IEEE Transactions on , vol.46, no.11, pp.3459-3471, Nov. 2008

[17] Pau Serra Morales; , "PROCESSAT DE DADES I ESTIMACIÓ D'ERRORS EN UN SISTEMA SAR BIESTÀTIC AMB RECEPTOR FIX," Projecte fi de carrera-Universitat Politècnica de Catalunya. Departament de Teoria del Senyal i Comunicacions, 2007, Director: Dr. Paco López Dekker, UPC Library catalog: PFC 07/140

[18] Cumming, Ian; , ”Digital processing of synthetic aperture radar data : algorithms and implementation / Ian G. Cumming, Frank H. Wong”, Chapter 13: Azimuth FM Rate Estimation, page 576 - 578, Boston : Artech House, cop. 2005

[19] By Michael O. Kolawole: , “Radar systems, peak detection and tracking”, section 10.3 : Matched Filter, page 281, Newnes, 2002

A. Appendix

The results obtained under this thesis for Acquisition 2 (July 02, 2010) have been presented at the EUSAR conference, Aachen Germany, 2010. It's citation is:

"A. Broquetas, P. Lopez-Dekker, J.J. Mallorquí, A. Aguasca, M. Fortes. J.C. Merlano, S. Duque, M. A. Siddique, "**SABRINA-X: Bistatic SAR receiver for TerraSAR-X**", Proceedings of EUSAR-2010, Aachen, Germany."

The system design of SABRINA-X and the results of the Acquistion 1 (April 03, 2010) have been accepted for publication in IEEE International Geoscience and Remote-sensing Symposium (IGARSS) July, 2010. A copy of the publication is attached in the following pages.

BISTATIC SAR BASED ON TERRASAR-X AND GROUND BASED RECEIVERS

A.Broquetas, M.Fortes, M.A.Siddique, S.Duque, J.C.Merlano, P.Lopez-Dekker(*), J.J. Mallorquí, A.Aguasca

RSLab, Universitat Politècnica de Catalunya, Campus Nord UPC - D3, 08034 Barcelona, Spain
(*) Now with DLR, HR Institute, Wessling, Germany

ABSTRACT

The paper presents the development of a ground based bistatic receiver using TerraSAR-X as a transmitter. The receiver subsystems like antennas, low-noise amplifiers, mixers, filters, synthesizers, etc. have been developed using low-cost monolithic devices in order to allow affordable deployment and at the same time offer final year students a challenging SAR engineering project. First raw data have been acquired on the Barcelona harbor area that has been focused producing geocoded images well matched with existing maps. A preliminary interferogram have been also produced.

1. INTRODUCTION

Bistatic systems are emerging as a new SAR research field opening the possibility to explore alternative geometries and different scattering mechanisms. Some of the upcoming systems, such as the recently launched Tandem-X mission, can be described as quasi-monostatic, with the receiver and the transmitter close to each other in almost parallel orbits. In contrast, if the receiver and the transmitter follow independent trajectories or are located far apart completely, new scenarios arise. Besides the geometry-related issues in the design of bistatic systems, there are a number of synchronization-related challenges. For example, the needs for independent reference oscillators on transmit and receive increases the impact of oscillator phase noise. Experimental studies are being carried out to study some specific aspects of bistatic SAR systems, including scattering phenomena, raw data processing, hardware related aspects with a particular emphasis on those linked to synchronization, interferometry and polarimetry [|1], [2].

This paper presents the SABRINA-X bistatic receiver, its main design parameters and the preliminary results obtained. The first data takes have been carried out on the Barcelona harbor area from a nearby hill site. A first bistatic image has been focused and geocoded and is accurately matched to the ground truth including some anchored ships. A preliminary single pass interferometric image has been obtained using two stacked antennas. Fringes both on ground and sea surface can be observed in spite of the low reflectivity inner water surface of the harbor. With the exception of commercial digitizers, this receiver has been fully developed from discrete and monolithic devices by undergraduate and graduate students in the context of final year remote sensing engineering projects resulting in a low cost receiver.

2. SABRINA-X RECEIVER

SABRINA-X is a coherent homodyne receiver tuned at TerraSAR-X 9.65 GHz carrier. To obtain a low phase noise the local oscillator signal is obtained from a ultra-low noise crystal reference oscillator and a subharmonic low noise PLL followed by an active x4 frequency multiplier. The resulting LO signal is amplified by a driver stage to reach the recommended levels (+13 dBm) of each channel I/Q mixers.

I/Q operation allow doubling the RF bandwidth with respect to digitzers maximum acquisition frequency. In the case of the nominal 150 MHz bandwidth of TerraSAR-X an acquisition at 100 Ms/s speed and low-pass antialiasing filters of 70 MHz have been adopted for the first bistatic signal acquisitions.

Operation in low IF ADC acquisition is also possible modifying the LO frequency setting at one side of the RF band but requires higher sampling speed. The advantage of low IF acquisition is that only one ADC is required per channel and there is no need to compensate for possible I/Q mixer amplitude and phase unbalances.

Low noise amplifiers with a typical gain of 19 dB are used in the receivers front-ends in order to keep the noise figure below 3 dB. The received signal is bandpass filtered in order to reject possible out of band intereferences. A microstrip coupled lines filter with 3 resonators has been designed for this purpose having an insertion loss of 3 dB and 300 MHz bandwidth suitable for both nominal and extended bandwidth TerraSAR-X operation. To compensate for filter insertion loss and increase the chain RF gain a second amplifier with a gain of 14 dB is used between the filter output and I/Q mixer input as shown in Fig. 1. After I/Q detection both base-band I,Q signals are low-pass filtered with a cut-off frequency of 70 MHz and amplified with a low-noise wide band DC-1GHz amplifier with 16.5 dB gain.

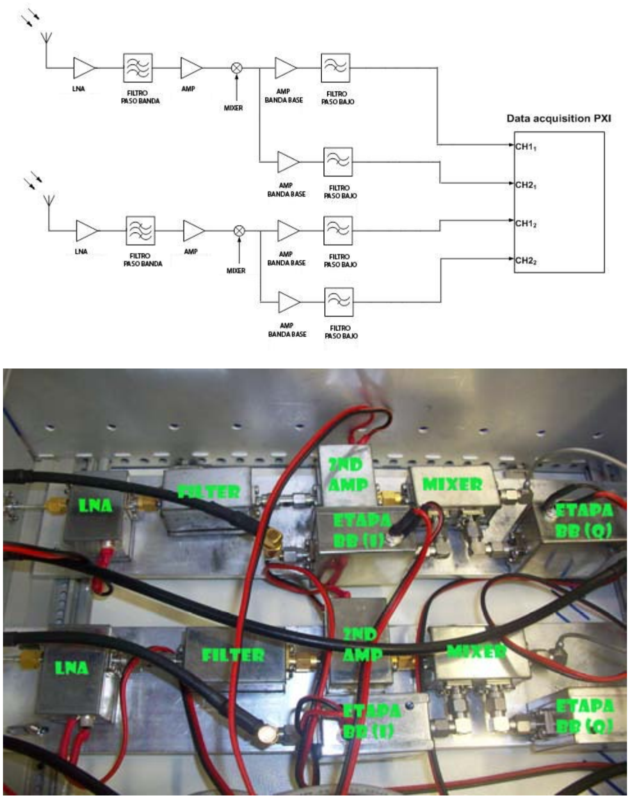

Figure 1 SABRINA-X bistatic receiver diagram and physical layout showing 2 RF channels

After amplification the output receiver ports deliver the base-band signals to a commercial PXI-based digitizer with 12 bit of resolution. The onboard memory allows 2.5 seconds of continuous signal acquisition which is sufficient for bistatic close to ground applications if precise orbital data is used. Figures 1 and 2 show the developed receiver with the first 2 homodyne I/Q channels, intended for direct and reflected signal simultaneous acquisitions using synchronous digitizing boards.

Using simple rectangular horn antennas with a gain of 18 dB, the direct signal is acquired with a signal to noise ratio close to 40 dB in the center of the TerraSAR-X beam. In the case of the reflected channel the Noise Equivalent σ^0 is -25 dB for an observed area at around 1 km distance from the receiver.

It must be pointed out that bistatic radar scattering coefficients are expected to be different from monostatic values depending on the detailed scene surface. For example in urban areas the strong monostatic returns corresponding to trihedrals and dihedrals formed by building walls and underlying flat surfaces should not be present in a bistatic geometry, however other strong scatterers related to single or multiple surfaces can appear. More bistatic radar observations are needed in combination monostatic images and ground truth analysis to understand the dominant bistatic scattering mechanisms in both natural and man-made surfaces.

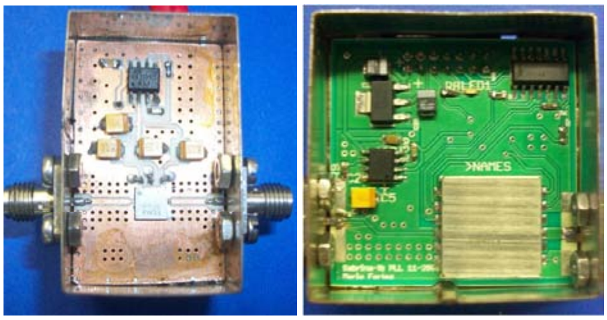

Figure 2 SABRINA-X LNA and LO/4 synthesizer

3. FIRST DATA ACQUISTIONS

After laboratory tests and receiver calibration a first data take of a TerraSAR-X illumination over the UPC campus showed the expected direct signal envelope depicted in Fig. 3. This experiment revealed a correct acquisition timing showing the main lobe of TerraSAR-X close to the center of the observation time window (Fig.3). Since the receiving antenna has a much wider beamwidth, the pattern shown in Fig.3 corresponds basically to the azimuth cut of TerraSAR-X operating beam. In normal operation TerraSAR-X transmitting array is configured with no tapering, for this reason the captured pattern shows the expected sinc shape.

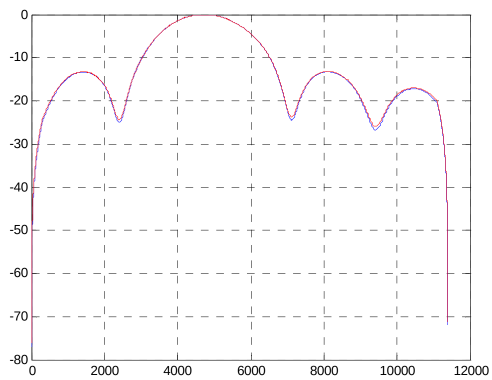

Figure 3 TerraSAR-X direct signal envelope (dB) vs. azimuth sample number (PRF) captured by SABRINA-X

A second experiment has been carried out recently on the Barcelona harbor area where the proximity of a hill allows a suitable site of opportunity with a view of some buildings, quays, ships, and calm sea water. In this case the two available channels where configured to record 3 signals: direct path, scattered low and scattered high antennas of an interferometric vertical stack for single-pass configuration. The lack of 3 channels was circumvented by adding the direct signal to one of the scattered signals with a 1:2 power splitter and a 6 dB attenuator on the direct branch to reduce the dynamic range between these two signals. After pulse compression the delay of the scattered signals was expected to offer a satisfactory separation of both direct and scattered contributions. The scattering receiving antennas where stacked vertically with a separation of 1118 mm as shown in Fig. 4.

Figure 4 Sabrina-X with 3 antennas configured for interferometric acquisition over harbor area

To carry out the bistatic SAR processing, first the linear complex data take has to be converted in the usual SAR 2D matrix. This can be done easily once the direct channel data is range compressed and the resulting peak positions are used as time reference of the scattered signal. Fast preliminary processing can be performed using the direct data signal is used both for range and azimuth compression of the scattered data since the phase history of the direct channel is very similar to the phase history of scatterers close to the receiver antennas. A more refined processing is based on precise time alignment and Range Cell Migration polynomial fitting. In this case the frequency offset between TSX and SABRINA is estimated from the pulse to pulse phase change once compensated for RCM in comparison with expected phase history [2].

Figure 5 show the acquisition site position in a optical zenithal view of the harbor area, the arrows indicate the azimuthal pointing of the direct (blue) and scattered (black) signal antennas.

Figure 5 Acquisition site of Sabrina-X on the Montjuich hill close to the harbor area.

Figure 6 Scene of harbor at the acquisition time window from the acquisition point

Fig. 6 shows a photograph of the scene at the time of data acquisition in the direction of bistatic observation. Note the presence of a large ship, and cargo trucks at front area and both sides of the quay. Fig. 7 shows the amplitude bistatic geocoded image with very good agreement with harbor detailed map available from the catalan mapping agency (ICC). Note the strong scattering centers produced by metallic cargo trucks, buildings and ship within the cone covered by the horn antennas. Also the calm water surface can be observed except in the quays shadowed areas.

A first single pass interferometric image has been obtained after phase subtraction, filtering and geocoding (Fig. 8). Note that coherence is maintained on the water surface due to synchronous acquisition. The interferogram is affected however by strong sidelobes from direct signal and the brightest nearby scattering centers. Accurate range compression requires a replica of the transmitted pulse which contains higher order terms with respect and ideal chirp [3]. In this experiment however the replica could not be obtained with the desired accuracy due to contamination of the direct uncompressed pulse by the scattered signal.

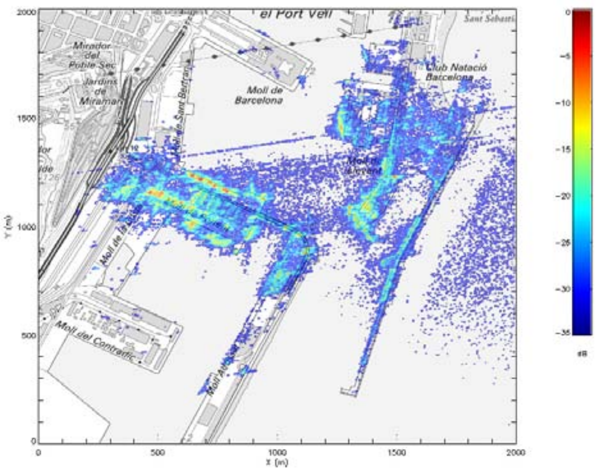

Figure 7 Geocoded amplitude image of the harbor overlaid on the city topographic map

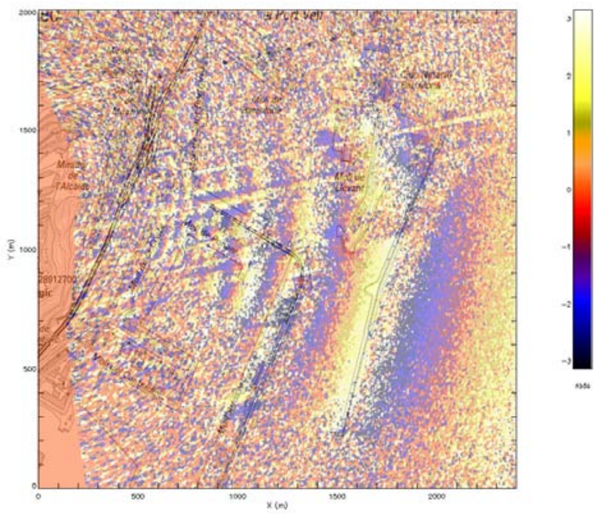

Figure 8 Geocoded phase image overlaid on harbor topographic map without DEM compensation.

The systematic slope due to the slant observation has been removed in Fig.9 using a smoothed DEM of the harbor area. Phase changes due to quays relief, buildings and ships can be observed.

4. CONCLUSIONS

SABRINA-X has been developed for bistatic SAR acquisition using TSX and other X-Band SAR satellites. A first image on the Barcelona harbor has shown correct PRF and carrier synchronism after data preprocessing. Both amplitude and interferometric images have been obtained with good agreement with ground truth. Exploitation of fixed bistatic SAR is strongly conditioned by satellite mission planning and availability of suitable sites of opportunity.

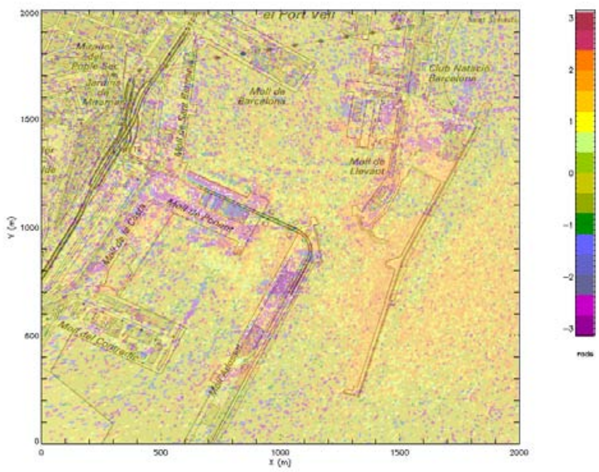

Figure 9 Geocoded phase image overlaid on habor topographic map after filtering and low resolution DEM phase removal.

Acknowledgment: This work has been supported by the DLR TSX Science Proposal MTH0561 and the Spanish Ministerio de Ciencia e Innovación, Project: TEC2008-06764-C02-01

5. REFERENCES

[1] J. Sanz-Marcos, P. Lopez-Dekker, J.J. Mallorqui, A. Aguasca, P. Prats, "SABRINA: A SAR Bistatic Receiver for Interferometric Applications", IEEE Geoscience and Remote Sensing Letters, Volume 4, Issue 2, April 2007, Page(s):307 – 311

[2] P. Lopez-Dekker, J.J. Mallorqui, P. Serra-Morales, J. Sanz-Marcos, "Phase Synchronization and Doppler Centroid Estimation in Fixed Receiver Bistatic SAR Systems", IEEE Transactions on Geoscience and Remote Sensing, Volume 46, Issue 11, Part 1, Nov. 2008 Page(s):3459 – 3471.

[3] A. Broquetas, P. Lopez-Dekker, J.J. Mallorquí, A.Aguasca, M.Fortes. J.C.Merlano, S.Duque, M.A.Siddique, "SABRINA-X: Bistatic SAR receiver for TerraSAR-X", Proceedings of EUSAR-2010, Aachen, Germany.